Journal of Sound and Vibration 329 (2010) 1924–1953

Contents lists available at ScienceDirect

Journal of Sound and Vibration

journal homepage: www.elsevier.com/locate/jsvi

# A new formulation and error analysis for vibrating dam–reservoir systems with upstream transmitting boundary conditions

Najib Bouaanani *, Benjamin Miquel

*Department of Civil, Geological and Mining Engineering, École Polytechnique de Montréal, Montréal, Canada QC H3C 3A7*

ARTICLE INFO

*Article history:*
Received 28 January 2009
Received in revised form
1 December 2009
Accepted 3 December 2009
Handling Editor: H. Ouyang
Available online 8 January 2010

ABSTRACT

This paper proposes and validates a new formulation to investigate the dynamic response of dam–reservoir systems with upstream transmitting boundary conditions (TBCs). The mathematical derivations are provided for the new formulation as well as for exact and various approximate TBCs. The developed analytical equations can be solved numerically to assess the accuracy of a given TBC and determine the associated error independently of FEM or BEM modeling of the reservoir. The method is first validated in the case of semi-infinite reservoirs and an excellent agreement is obtained against classical techniques. The paper presents a fundamental understanding of the behavior of various TBCs and a systematic identification of their influence on the system's dynamic response, considering: (i) dam flexibility, (ii) water compressibility, (iii) reservoir bottom wave absorption, (iv) reservoir truncation length, and (v) excitation frequency. The new method is used to obtain exact error estimators to evaluate the effects of various TBCs on the dam–reservoir first resonant frequency and hydrodynamic forces acting on the dam upstream face. The proposed formulation can be programmed easily and used efficiently for rigorous assessment of classical or newly developed TBCs for vibrating dam–reservoir systems or similar fluid–structure problems.



## 1. Introduction

Accurate evaluation of reservoir loading on a dam upstream face is crucial for its seismic safety assessment. Significant research has been devoted to study this type of loading since the pioneering work of Westergaard [1] who used a heightwise added mass distribution to model hydrodynamic pressure on a dam upstream face. This concept has been widely used for several decades to design earthquake resistant gravity dams. More advanced analytical and numerical frequency-domain and time-domain approaches were proposed later to account for dam deformability, water compressibility and reservoir bottom wave absorption in the seismic response of dam–reservoir systems [2–13]. Some of these procedures were validated against forced-vibration testing of concrete gravity and arch dams [14–16]. Among the numerical techniques used to study dam–reservoir systems, the finite element method (FEM) and boundary element method (BEM) have gained wide popularity. Due to the large extent of the reservoir, these methods require its virtual truncation at a finite distance from dam face and application of appropriate transmitting boundary conditions (TBCs) at the upstream end of the reservoir. Here, we note that although BEM may intrinsically satisfy radiation conditions at infinity contrary to FEM, to reduce computational burden, it might be useful to split an infinite reservoir into: (i) a finite near field

* Corresponding author.
*E-mail address:* najib.bouaanani@polymtl.ca (N. Bouaanani).

0022-460X/$ - see front matter © 2009 Elsevier Ltd. All rights reserved.
doi:10.1016/j.jsv.2009.12.005

region to be discretized by BEM, and (ii) an infinite far-field region, to be modeled as an infinite continuum domain or by infinite finite elements [11]. In this case, as for FEM, a TBC has to be applied at the boundary between the near field and the far field to ensure adequate energy radiation at infinity. These special boundary conditions and the truncation distance should be defined appropriately to prevent reflection of spurious waves back towards the dam. Otherwise, significant error may be introduced in the prediction of the dynamic response of the dam–reservoir system.

Among the many TBCs proposed in the literature, the Sommerfeld radiation boundary condition has been widely used [17–20]. Although the method can be easily incorporated in a FEM or BEM program, it performs adequately only when placed at a large distance from dam face. Saini et al. [8] and Saini [21] studied the coupled response of dam–reservoir systems and developed infinite elements to model energy dissipation at the far-upstream end of the reservoir. They concluded that the effect of radiation damping is significant at high frequencies of excitation. Hall and Chopra [5] developed a substructuring technique where the dam, reservoir and foundation are modeled using finite elements and their responses coupled through interface forces to obtain the global dynamic behavior. They considered a one-dimensional model to account for reflection of waves at reservoir bottom, and proposed a one-dimensional infinite boundary condition to simulate absorption of compression waves outgoing from a seismically excited dam–reservoir towards its upstream end. Humar and Roufaiel [22] proposed a modified Sommerfeld boundary condition, implemented it into a finite element program and proved its efficiency to be superior to the classical Sommerfeld TBC for frequencies between the first and the second natural frequencies of the reservoir. They did not consider reservoir bottom wave absorption in their study. Neglecting water compressibility, Sharan [23] proposed a TBC based on the analytical solution for hydrodynamic pressure in a reservoir impounded by a rigid dam. He concluded that this TBC gives satisfactory results even for very short reservoir truncation lengths. Sharan [24] extended his TBC to include water compressibility, but still considered a complete reflective reservoir bottom and a rigid dam. He showed that the new TBC is a generalization of the Sommerfeld TBC and of that proposed by Humar and Roufaiel [22]. He also confirmed that the Sommerfeld TBC gives satisfactory results only when placed very far away from dam face and for excitation frequencies lower than the reservoir first natural frequency. Sharan [25] extended the use of his TBC to deformable dams by dividing the reservoir into a near-field domain with an arbitrary shape, and a far-field domain with a uniform rectangular geometry. He modeled the whole dam–reservoir system using finite elements and applied a TBC based on a rigid dam assumption to the upstream end of the far-field domain. The TBC was improved later by including the effects of reservoir bottom wave absorption [26]. Satisfactory results were obtained for short truncation lengths and a wide range of excitation frequencies except near the second and third natural frequencies of the reservoir [26]. Jablonski [27] developed a BEM program implementing the TBC proposed by Hall and Chopra [5]. He studied the effect of the location of this TBC on hydrodynamic pressures at dam upstream face, and concluded that the accuracy of the results is sensitive to the type and size of the boundary elements used, a result also previously reported for finite element models [28,29].

All the TBCs described above were, however, developed considering a rigid dam assumption. Recently, Maity and Bhattacharyya [30] proposed a TBC that intrinsically takes account of dam flexibility and is therefore height-dependent. They considered a completely reflective reservoir bottom and implemented this TBC into a FEM program. They evidenced the effects of dam flexibility, and the TBC was shown efficient in time-domain analyses of dam–reservoir systems. Çetin and Mengi [31] developed a TBC based on spectral theory of waves propagating horizontally along a fluid reservoir with a completely reflective reservoir bottom. They assessed the TBC through BEM analysis of two benchmark problems of rigid dams subjected to harmonic and time dependent loadings. Bouaanani et al. [32] formulated a new TBC to account for energy radiation in ice-covered reservoirs, including the effects of reservoir bottom wave absorption and water compressibility. They implemented the proposed TBC into a BEM program and proved its effectiveness and accuracy through a parametric study of a typical dam–reservoir system. Maity [33] and Küçükarslan [34] proposed TBCs to study earthquake-induced horizontal vibrations of incompressible-unbounded infinite fluid domains with completely reflective reservoir bottoms. They incorporated the TBCs into FEM programs and showed their performance to be superior to classical TBCs when placed near dam upstream face. Gogoi and Maity [35] extended the TBC proposed by Maity and Bhattacharyya [30] to include energy dissipation at reservoir bottom. They defined the new TBC based on a closed-form formulation of hydrodynamic pressure proposed by Bouaanani et al. [36]. The proposed TBC was implemented in a FEM code for frequency- and time-domain analyses of dam–reservoir systems and was found to perform efficiently on a wide frequency range of interest in dam seismic analyses.

TBCs are generally approximate, absorbing only a portion of impinging waves, and thus introducing some error into the solution. This error is usually to be minimized based on the experience and judgement of the analyst after some initial guess of the truncation boundary location. Successive trials are then performed to ensure numerical convergence of the FEM or BEM solutions as a function of truncation length and mesh refinement. It is important, however, to separate errors that can be attributed strictly to the type of TBC applied and its location from the discretization, convergence, or other numerical or modeling errors specific to the FEM or BEM packages used. Such a validation is generally conducted through comparison with the exact solution of the mathematical model describing dam–reservoirs with upstream TBCs. However, available analytical solutions can handle only heightwise constant TBCs and thus cannot be used to validate FEM or BEM models with height-dependent TBCs which include dam flexibility effects. The main objective of this work is to develop an original and rigorous analytical technique to reliably predict the accuracy of a given TBC in a vibrating dam–reservoir system and estimate the TBC effects and associated error independently of FEM or BEM modeling of the reservoir. This method would be also useful in testing, validating or developing either frequency-dependent TBCs

or frequency-independent TBCs which are generally more suitable for time domain analyses of dam–reservoir systems. Another objective of this work is to use the proposed method to present a fundamental understanding of the behavior of various TBCs and provide a systematic identification of their influence on the dynamic response of a dam–reservoir system, considering the effects of: (i) dam flexibility, (ii) water compressibility, (iii) reservoir bottom wave absorption, (iv) reservoir truncation length, and (v) excitation frequency. To the authors' knowledge, such a thorough analysis has never been published.

This paper is organized as follows. In Section 2, we briefly review the mathematical background of a classical analytical technique and we define some common TBCs. We then establish the mathematical formulation underlying the new analytical method proposed to study dam–reservoir systems with upstream TBCs. In Section 3, we examine the sensitivity of common TBCs to various key factors, and we illustrate the use of the proposed method to investigate the efficiency and accuracy of these TBCs. The last section contains some concluding remarks.

## 2. Mathematical formulations

### 2.1. Review of the formulation for a semi-infinite reservoir

Fig. 1(a) illustrates a typical gravity dam of height $H_s$, impounding a rectangular semi-infinite reservoir of constant height $H_r$. The effects of sediments that may be deposited at reservoir bottom are also considered. A Cartesian coordinate system with axes $x$ and $y$ and origin at the heel of the structure is adopted as well as the following main assumptions: (i) the dam and the water are assumed to have a linear elastic behavior; (ii) the water in the reservoir is compressible and inviscid, with its motion irrotational and limited to small amplitudes; and (iii) gravity surface waves are neglected. Under these assumptions, the hydrodynamic pressure $p(x,y,t)$ in the reservoir obeys the wave equation

$$\nabla^2 p = \frac{1}{C_r^2}\frac{\partial^2 p}{\partial t^2} \tag{1}$$

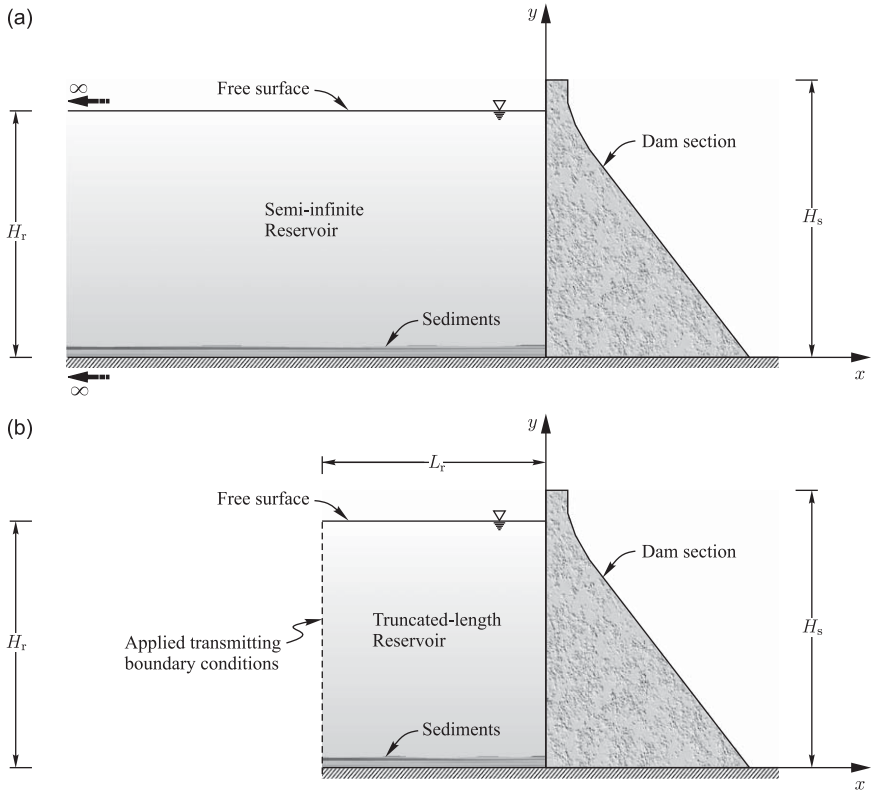


**Fig. 1.** Dam–reservoir systems considered for the analytical formulation: (a) dam impounding a semi-infinite reservoir; (b) dam impounding a truncated-length reservoir.

where $\nabla^2$ is the Laplace differential operator, $t$ the time variable, $\rho_r$ the mass density of water and $C_r$ the compression wave velocity given by

$$C_r = \sqrt{\frac{\mu_r}{\rho_r}} \tag{2}$$

in which $\mu_r$ denotes the bulk modulus of water.

Considering horizontal harmonic ground accelerations $\ddot{u}_g(t) = a_g e^{i\omega t}$, the hydrodynamic pressure in the reservoir can be expressed in the frequency domain as $p(x,y,t) = \overline{p}(x,y,\omega)e^{i\omega t}$, where $\overline{p}(x,y,\omega)$ is a complex-valued frequency response function (FRF). Introducing this transformation into Eq. (1) yields the classical Helmholtz equation

$$\nabla^2\overline{p} + \frac{\omega^2}{C_r^2}\overline{p} = 0 \tag{3}$$

The dam section can be modeled using finite elements and assuming that the system has a constant hysteretic damping, the dynamic equilibrium of the dam–reservoir system can be expressed in the frequency domain as

$$[-\omega^2\mathbf{M} + (1+i\eta_s)\mathbf{K}]\overline{\mathbf{U}}(\omega) = -a_g\mathbf{M}\mathbf{1} + \overline{\mathbf{F}}_h(\omega) \tag{4}$$

where $\overline{\mathbf{U}}$ is a column-vector containing the FRFs of dam nodal displacements relative to the ground, $\mathbf{M}$ and $\mathbf{K}$ are the dam mass and stiffness matrices, respectively, $\eta_s$ is the structural hysteretic damping factor, $\overline{\mathbf{F}}_h$ is a column-vector containing the FRFs of hydrodynamic pressure loads, and $\mathbf{1}$ is a column-vector with the same dimension as the vector of nodal relative displacements, containing zeros except along horizontal degrees of freedom which correspond to the direction of earthquake excitation. Using a modal superposition analysis, the FRFs of relative displacement and acceleration components at coordinate $(x,y)$ can be expressed as

$$\overline{u}(x,y,\omega) = \sum_{j=1}^{m_s}\psi_j^{(x)}(x,y)\overline{Z}_j(\omega); \quad \ddot{\overline{u}}(x,y,\omega) = -\omega^2\sum_{j=1}^{m_s}\psi_j^{(x)}(x,y)\overline{Z}_j(\omega) \tag{5}$$

$$\overline{v}(x,y,\omega) = \sum_{j=1}^{m_s}\psi_j^{(y)}(x,y)\overline{Z}_j(\omega); \quad \ddot{\overline{v}}(x,y,\omega) = -\omega^2\sum_{j=1}^{m_s}\psi_j^{(y)}(x,y)\overline{Z}_j(\omega) \tag{6}$$

where $\overline{u}$ and $\overline{v}$ denote the horizontal and vertical relative displacements, respectively, $\ddot{\overline{u}}$ and $\ddot{\overline{v}}$ the horizontal and vertical accelerations, respectively, $\psi_j^{(x)}$ and $\psi_j^{(y)}$ the $x$- and $y$-components of the $j$ th dam mode shape, $\overline{Z}_j$ the generalized coordinate, and $m_s$ the number of structural mode shapes included in the analysis. The hydrodynamic pressure FRF $\overline{p}$ can be decomposed as [6]

$$\overline{p}(x,y,\omega) = \overline{p}_0(x,y,\omega) - \omega^2\sum_{j=1}^{m_s}\overline{Z}_j(\omega)\overline{p}_j(x,y,\omega) \tag{7}$$

where $\overline{p}_0$ is the FRF for hydrodynamic pressure due to rigid body motion of the dam, and where $\overline{p}_j$ is the FRF corresponding to hydrodynamic pressure due to horizontal acceleration $\psi_j^{(x)}(y) = \psi_j^{(x)}(0,y)$ of the dam upstream face along structural mode $j$. The boundary conditions to be satisfied by FRFs $\overline{p}_0$ and $\overline{p}_j$ are detailed in this section.

- *At dam–reservoir interface*: This boundary condition is based on compatibility between hydrodynamic pressures and normal displacements at dam–reservoir interface, yielding [6]

$$\frac{\partial\overline{p}_0}{\partial x}(0,y,\omega) = -\rho_r a_g; \quad \frac{\partial\overline{p}_j}{\partial x}(0,y,\omega) = -\rho_r\psi_j^{(x)}(y) \tag{8}$$

- *At reservoir free surface*: Neglecting the effect of gravity waves at reservoir free surface [38,39], hydrodynamic pressures at this location are assumed null

$$\overline{p}_0(x,H_r,\omega) = \overline{p}_j(x,H_r,\omega) = 0 \tag{9}$$

- *At reservoir bottom*: This boundary condition was introduced by Hall and Chopra [5] to approximately account for energy dissipation at reservoir bottom through one-dimensional partial absorption of incident compression waves normal to the reservoir bottom boundary

$$\frac{\partial\overline{p}_0}{\partial y}(x,0,\omega) = i\omega q\overline{p}_0(x,0,\omega); \quad \frac{\partial\overline{p}_j}{\partial y}(x,0,\omega) = i\omega q\overline{p}_j(x,0,\omega) \tag{10}$$

where $q$ is a damping coefficient defined at the reservoir bottom as

$$q = \frac{\rho_r}{\rho_f C_f} \tag{11}$$

and where $\rho_f$ and $C_f$ denote the mass density and the compression wave velocity within the reservoir foundation, respectively. The portion of the wave amplitude reflected back to the reservoir is represented by the wave reflection

coefficient $\alpha$ defined by

$$\alpha = \frac{1-qC_r}{1+qC_r} \tag{12}$$

where $\alpha$ may vary from 0 for full wave absorption to 1 for full wave reflection.

- *At infinity upstream of the reservoir*: To obtain analytical expressions for the FRFs $\overline{p}_0$ and $\overline{p}_j$, Hall and Chopra [5] and Fenves and Chopra [6] considered an undisturbed pressure condition implying a null hydrodynamic pressure at infinity of the continuum fluid domain upstream, i.e. when $x\to-\infty$ according to the system of axes in Fig. 1(a):

$$\lim_{x\to-\infty}\overline{p}_0(x,y,\omega)=\lim_{x\to-\infty}\overline{p}_j(x,y,\omega)=0 \tag{13}$$

In the rest of the paper, a superscript $^{(\infty)}$ will be used to denote hydrodynamic pressures, forces and other physical quantities determined using the aforementioned boundary conditions. These boundary conditions are coupled to Eq. (3) to determine classical expressions of hydrodynamic pressure [6]. The resulting FRFs $\overline{p}_0^{(\infty)}$ and $\overline{p}_j^{(\infty)}$ are written here as the summation of $m_r$ functions $\overline{p}_{0n}^{(\infty)}$ and $\overline{p}_{jn}^{(\infty)}$ corresponding each to a reservoir mode $n$

$$\overline{p}_0^{(\infty)}(x,y,\omega)=\sum_{n=1}^{m_r}\overline{p}_{0n}^{(\infty)}(x,y,\omega) \tag{14}$$

$$\overline{p}_j^{(\infty)}(x,y,\omega)=\sum_{n=1}^{m_r}\overline{p}_{jn}^{(\infty)}(x,y,\omega) \tag{15}$$

in which

$$\overline{p}_{0n}^{(\infty)}(x,y,\omega)=-2\rho_r a_g H_r\frac{\lambda_n^2(\omega)}{\beta_n(\omega)}\frac{I_{0n}(\omega)}{\kappa_n(\omega)}e^{\kappa_n(\omega)x}Y_n(y,\omega) \tag{16}$$

$$\overline{p}_{jn}^{(\infty)}(x,y,\omega)=-2\rho_r H_r\frac{\lambda_n^2(\omega)}{\beta_n(\omega)}\frac{I_{jn}(\omega)}{\kappa_n(\omega)}e^{\kappa_n(\omega)x}Y_n(y,\omega) \tag{17}$$

where $\lambda_n$ and $Y_n$ are complex-valued frequency dependent eigenvalues and orthogonal eigenfunctions satisfying for each reservoir mode $n$

$$e^{2i\lambda_n(\omega)H_r}=-\frac{\lambda_n(\omega)-\omega q}{\lambda_n(\omega)+\omega q} \tag{18}$$

$$Y_n(y,\omega)=\frac{[\lambda_n(\omega)-\omega q]e^{-i\lambda_n(\omega)y}+[\lambda_n(\omega)+\omega q]e^{i\lambda_n(\omega)y}}{2\lambda_n(\omega)} \tag{19}$$

and where the terms $\beta_n$, $\kappa_n$, $I_{0n}$, $I_{jn}$ are given by

$$\beta_n(\omega)=H_r[\lambda_n^2(\omega)-\omega^2q^2]+i\omega q;\quad \kappa_n(\omega)=\sqrt{\lambda_n^2(\omega)-\frac{\omega^2}{C_r^2}} \tag{20}$$

$$I_{0n}(\omega)=\frac{1}{H_r}\int_0^{H_r}Y_n(y,\omega)dy;\quad I_{jn}(\omega)=\frac{1}{H_r}\int_0^{H_r}\psi_j^{(x)}(y)Y_n(y,\omega)\,dy \tag{21}$$

Iterative techniques such as Newton–Raphson method can be used to solve Eq. (18) at each excitation frequency $\omega$. We note that for a completely reflective reservoir bottom, i.e. $\alpha=1$, $\kappa_n(\omega)$ is either: (i) a real positive number when exciting frequency $\omega$ is lower than the vibration frequency $\omega_{rn}$ of the impounded reservoir, or (ii) a pure imaginary number otherwise [5,6,22]. In the first case, the sums in Eqs. (14) and (15) decay exponentially with increasing distance upstream, and in the second case, these sums contain a non-decaying part representing waves propagating in the upstream direction. When reservoir bottom absorption is included, $\kappa_n$ is a complex number with a positive real part, and the series in Eqs. (14) and (15) decay with increasing distance upstream, although slowly for slightly absorptive reservoirs. The number of reservoir modes $m_r$ to be included in the analysis should be selected based on the convergence of the sums in Eqs. (14) and (15). Through extensive numerical analyses of idealized dam sections, Fenves and Chopra [6] proposed and validated a minimum value $m_r>\omega_{\max}/(2\omega_0)+5$ to ensure convergence, where $\omega_{\max}$ denotes the maximum excitation frequency considered in the analysis, and $\omega_0=\pi C_r/(2H_r)$ the natural frequency of the full semi-infinite reservoir.

If water compressibility is neglected, real-valued and frequency-independent eigenvectors $\lambda_n$ and eigenvectors $Y_n$ are given by

$$\lambda_n=\frac{(2n-1)\pi}{2H_r};\quad Y_n(y)=\cos\left[\frac{(2n-1)\pi y}{2H_r}\right] \tag{22}$$

and Eqs. (20) and (21) simplify to

$$\beta_n = \frac{(2n-1)^2\pi^2}{4H_r}; \quad \kappa_n = \frac{(2n-1)\pi}{2H_r} \tag{23}$$

$$I_{0n} = 2\frac{(-1)^{n-1}}{(2n-1)\pi}; \quad I_{jn} = \frac{1}{H_r}\int_0^{H_r} \psi_j^{(x)}(y)\cos\left[\frac{(2n-1)\pi y}{2H_r}\right] \mathrm{d}y \tag{24}$$

yielding the hydrodynamic pressures

$$\overline{p}_{0n}^{(\infty)}(x,y) = -8\rho_r a_g H_r \frac{(-1)^{n-1}\cos\left[\frac{(2n-1)\pi y}{2H_r}\right]}{(2n-1)^2\pi^2} \mathrm{e}^{\kappa_n x} \tag{25}$$

$$\overline{p}_{jn}^{(\infty)}(x,y) = -4\rho_r \frac{\cos\left[\frac{(2n-1)\pi y}{2H_r}\right]}{(2n-1)\pi} \mathrm{e}^{\kappa_n x} \int_0^{H_r} \psi_j^{(x)}(y)\cos\left[\frac{(2n-1)\pi y}{2H_r}\right] \mathrm{d}y \tag{26}$$

Depending on whether water compressibility is included or not, Eqs. (16) and (17) or Eqs. (25) and (26) are used to obtain hydrodynamic pressures $\overline{p}_0^{(\infty)}$ and $\overline{p}_j^{(\infty)}$. The FRF for total hydrodynamic pressure is then given by [Eq. (7)]

$$\overline{p}^{(\infty)}(x,y,\omega) = \overline{p}_0^{(\infty)}(x,y,\omega) - \omega^2 \sum_{j=1}^{m_s} \overline{Z}_j^{(\infty)}(\omega)\overline{p}_j^{(\infty)}(x,y,\omega) \tag{27}$$

where the vector $\overline{\mathbf{Z}}^{(\infty)}$ of generalized coordinates $\overline{Z}_j^{(\infty)}$, $j = 1 \ldots m_s$, is obtained by solving the system of equations

$$\overline{\mathbf{S}}^{(\infty)}\overline{\mathbf{Z}}^{(\infty)} = \overline{\mathbf{Q}}^{(\infty)} \tag{28}$$

in which elements of matrices $\overline{\mathbf{S}}^{(\infty)}$ and $\overline{\mathbf{Q}}^{(\infty)}$ are obtained for $n = 1 \ldots m_s$ and $j = 1 \ldots m_s$ as

$$\overline{S}_{nj}^{(\infty)}(\omega) = [-\omega^2 + (1+\mathrm{i}\eta_s)\omega_n^2]\delta_{nj} + \omega^2 \int_0^{H_r} \overline{p}_j^{(\infty)}(0,y,\omega)\psi_n^{(x)}(y)\,\mathrm{d}y \tag{29}$$

$$\overline{Q}_n^{(\infty)}(\omega) = -a_g \boldsymbol{\psi}_n^{\mathrm{T}}\mathbf{M}\mathbf{1} + \int_0^{H_r} \overline{p}_0^{(\infty)}(0,y,\omega)\psi_n^{(x)}(y)\,\mathrm{d}y \tag{30}$$

where $\delta$ denotes the Kronecker symbol and $\omega_n$ is the vibration frequency corresponding to structural mode shape $\psi_n$. A convergence study is conducted to determine the sufficient numbers $m_s$ and $m_r$ of structural and reservoir mode shapes to be included into each specific analysis. We can also define the FRFs for hydrodynamic forces applied on dam upstream face, i.e. at $x = 0$ according to the system of axes in Fig. 1

$$\overline{F}_0^{(\infty)}(\omega) = \int_0^{H_r} \overline{p}_0^{(\infty)}(0,y,\omega)\,\mathrm{d}y; \quad \overline{F}^{(\infty)}(\omega) = \int_0^{H_r} \overline{p}^{(\infty)}(0,y,\omega)\,\mathrm{d}y \tag{31}$$

The formulation described in this section was originally developed by Fenves and Chopra [6] to investigate earthquake excited gravity dams impounding semi-infinite reservoirs. The method is based on a substructuring technique, where the dam is modeled using finite elements and where reservoir effects are accounted for analytically through hydrodynamic loads applied at dam upstream face and determined using mode shapes of the dam with an empty reservoir. Bouaanani and Lu [40] showed that this procedure to include dam–reservoir interaction yields excellent results when compared to techniques where the reservoir is modeled numerically using potential-based fluid finite elements. This analytical method will be referred to as the *classical* formulation in the rest of the paper and will serve as our reference solution.

### 2.2. New formulation considering transmitting boundary conditions

As mentioned previously, appropriate TBCs are required for efficient finite element or boundary element modeling of dam–reservoir systems. In this case, exact radiation boundary conditions at the far-dam upstream face [Eq. (13)] are replaced by TBCs to be applied at a finite distance $L_r$ from dam upstream face as shown in Fig. 1(b). TBCs are used to prevent or reduce reflection of waves impinging a fictitious truncation boundary of an infinite reservoir. They can be generally defined by the relationship between the hydrodynamic pressure and its normal gradient both determined at the truncation boundary. According to the system of axes in Fig. 1(b), we consider TBCs that can be expressed as

$$\frac{\partial \overline{p}_0^{(\infty)}}{\partial x}(-L_r,y,\omega) = \theta_0^{(L_r)}(y,\omega)\overline{p}_0^{(\infty)}(-L_r,y,\omega) \tag{32}$$

$$\frac{\partial \overline{p}_j^{(\infty)}}{\partial x}(-L_r,y,\omega) = \theta_j^{(L_r)}(y,\omega)\overline{p}_j^{(\infty)}(-L_r,y,\omega) \tag{33}$$

where the functions $\theta_0^{(L_r)}$ and $\theta_j^{(L_r)}$ are generally height- and frequency-dependent. We note that the TBC in Eq. (32) accounts for rigid body motion of the dam, while that in Eq. (33) accounts for dam elastic deformation along structural mode shape $\psi_j^{(x)}$. In the rest of the paper, a superscript $^{(L_r)}$ will be used to denote hydrodynamic pressures obtained using TBCs placed at a distance $L_r$ from dam upstream face. Differentiating Eq. (27) with respect to $x$ gives

$$\frac{\partial \overline{p}^{(\infty)}}{\partial x}(x,y,\omega)=\frac{\partial \overline{p}_0^{(\infty)}}{\partial x}(x,y,\omega)-\omega^2\sum_{j=1}^{m_s}\overline{Z}_j(\omega)\frac{\partial \overline{p}_j^{(\infty)}}{\partial x}(x,y,\omega) \tag{34}$$

Taking $x=-L_r$ and substituting Eqs. (32) and (33) into Eq. (34) yields

$$\frac{\partial \overline{p}^{(\infty)}}{\partial x}(-L_r,y,\omega)=\theta_0^{(L_r)}(y,\omega)\overline{p}_0^{(\infty)}(-L_r,y,\omega)-\omega^2\sum_{j=1}^{m_s}\overline{Z}_j(\omega)\theta_j^{(L_r)}(y,\omega)\overline{p}_j^{(\infty)}(-L_r,y,\omega) \tag{35}$$

Using Eqs. (27) and (35), we can define a TBC expressed in terms of total hydrodynamic pressure $\overline{p}^{(\infty)}$ as

$$\frac{\partial \overline{p}^{(\infty)}}{\partial x}(-L_r,y,\omega)=\theta^{(L_r)}(y,\omega)\overline{p}^{(\infty)}(-L_r,y,\omega) \tag{36}$$

in which the height- and frequency-dependent function $\theta^{(L_r)}$ is given by

$$\theta^{(L_r)}(y,\omega)=\frac{\theta_0^{(L_r)}(y,\omega)\overline{p}_0^{(\infty)}(-L_r,y,\omega)-\omega^2\sum_{j=1}^{m_s}\overline{Z}_j(\omega)\theta_j^{(L_r)}(y,\omega)\overline{p}_j^{(\infty)}(-L_r,y,\omega)}{\overline{p}_0^{(\infty)}(-L_r,y,\omega)-\omega^2\sum_{j=1}^{m_s}\overline{Z}_j(\omega)\overline{p}_j^{(\infty)}(-L_r,y,\omega)} \tag{37}$$

The TBCs defined by Eqs. (32)–(37) will be referred to as *analytical* TBCs in the rest of the paper. Using Eqs. (14) and (15), the functions $\theta_\ell^{(L_r)}$, $\ell=0,j$, can be expressed as

$$\theta_\ell^{(L_r)}(y,\omega)=\frac{\sum_{n=1}^{m_r}\kappa_n(\omega)\overline{p}_{\ell n}^{(\infty)}(-L_r,y,\omega)}{\sum_{n=1}^{m_r}\overline{p}_{\ell n}^{(\infty)}(-L_r,y,\omega)} \tag{38}$$

We will also examine the effectiveness of truncated TBCs, where the sum in Eq. (38) is truncated at a given number $\tilde{m}_r$ less than the number of reservoir modes $m_r$ ensuring convergence, yielding the function $\tilde{\theta}_\ell^{(L_r)}$

$$\tilde{\theta}_\ell^{(L_r)}(y,\omega)=\frac{\sum_{n=1}^{\tilde{m}_r}\kappa_n(\omega)\overline{p}_{\ell n}^{(\infty)}(-L_r,y,\omega)}{\sum_{n=1}^{\tilde{m}_r}\overline{p}_{\ell n}^{(\infty)}(-L_r,y,\omega)} \tag{39}$$

When water compressibility is neglected, Eq. (38) transforms to

$$\theta_\ell^{(L_r)}(y)=H_r\frac{\sum_{n=1}^{m_r}\lambda_n I_{\ell n}\cos(\lambda_n y)e^{-\lambda_n L_r}}{\sum_{n=1}^{m_r}\frac{I_{\ell n}}{\lambda_n}\cos(\lambda_n y)e^{-\lambda_n L_r}} \tag{40}$$

where $\lambda_n$ and $I_{\ell n}$ are determined according to Eqs. (22) and (24), respectively. We note that Eq. (40) also corresponds to very low frequencies, i.e. $\omega\to 0$, when water compressibility is included. In the rest of the paper, analytical TBCs will be distinguished as compressibility- or incompressibility-based depending on whether compressible or incompressible water assumptions are adopted.

When a TBC is applied at a finite length $L_r$, Eqs. (14)–(17) of the classical formulation are no longer valid to determine hydrodynamic pressure within the reservoir. To get a rigorous assessment of the accuracy and effectiveness of a given TBC, a new formulation is developed in this work. To alleviate the text, the detailed mathematical derivations of the formulation are presented in Appendix A. When TBCs in (32) and (33) are imposed at a distance $L_r$ from dam upstream face, we show in Appendix A that hydrodynamic pressures $\overline{p}_0^{(L_r)}$ and $\overline{p}_j^{(L_r)}$ can be expressed as

$$\overline{p}_0^{(L_r)}(x,y,\omega)=\sum_{n=1}^{m_r}\overline{p}_{0n}^{(L_r)}(x,y,\omega) \tag{41}$$

$$\overline{p}_j^{(L_r)}(x,y,\omega)=\sum_{n=1}^{m_r}\overline{p}_{jn}^{(L_r)}(x,y,\omega) \tag{42}$$

where FRFs $\overline{p}_{0n}^{(L_r)}$ and $\overline{p}_{jn}^{(L_r)}$ are given by

$$\overline{p}_{0n}^{(L_r)}(x,y,\omega)=\left\{[e^{-\kappa_n(\omega)x}+e^{\kappa_n(\omega)x}]\Gamma_n^{(0)}(\omega)-2\rho_r a_g H_r\frac{\lambda_n^2(\omega)}{\beta_n(\omega)}\frac{I_{0n}(\omega)}{\kappa_n(\omega)}e^{\kappa_n(\omega)x}\right\}Y_n(y,\omega)=[e^{-\kappa_n(\omega)x}+e^{\kappa_n(\omega)x}]\Gamma_n^{(0)}(\omega)Y_n(y,\omega)+\overline{p}_{0n}^{(\infty)}(x,y,\omega) \tag{43}$$

$$\overline{p}_{jn}^{(L_r)}(x,y,\omega)=\left\{[e^{-\kappa_n(\omega)x}+e^{\kappa_n(\omega)x}]\Gamma_n^{(j)}(\omega)-2\rho_r H_r\frac{\lambda_n^2(\omega)}{\beta_n(\omega)}\frac{I_{jn}(\omega)}{\kappa_n(\omega)}e^{\kappa_n(\omega)x}\right\}Y_n(y,\omega)=[e^{-\kappa_n(\omega)x}+e^{\kappa_n(\omega)x}]\Gamma_n^{(j)}(\omega)Y_n(y,\omega)+\overline{p}_{jn}^{(\infty)}(x,y,\omega) \tag{44}$$

in which $\Gamma_n^{(0)}(\omega)$ and $\Gamma_n^{(j)}(\omega)$ are elements of vectors $\mathbf{\Gamma}^{(0)}$ and $\mathbf{\Gamma}^{(j)}$, obtained by solving the systems of linear equations

$$\mathbf{A}^{(0)}(\omega)\mathbf{\Gamma}^{(0)}(\omega)=\mathbf{B}^{(0)}(\omega),\quad \mathbf{A}^{(j)}(\omega)\mathbf{\Gamma}^{(j)}(\omega)=\mathbf{B}^{(j)}(\omega) \tag{45}$$

where the elements of matrix $\mathbf{A}^{(\ell)}$ and vector $\mathbf{B}^{(\ell)}$ are given for $\ell=0,j$ by Eqs. (A.24) and (A.25) of Appendix A. Eqs. (A.24) and (A.25) will be used later to assess the efficiency of various TBCs and evaluate the associated errors. One important aspect of this formulation is that it takes account of the variations of the functions $\theta_0^{(L_r)}$ and $\theta_j^{(L_r)}$ over reservoir height. This dependence is investigated next. Using Eq. (38) the derivatives of the functions $\theta_\ell^{(L_r)}$, $\ell=0,j$, with respect to coordinate $y$ can obtained as

$$\frac{\partial\theta_\ell^{(L_r)}}{\partial y}(y,\omega)=\frac{\sum_{s=1}^{m_r}\sum_{n=1}^{m_r}[\kappa_s(\omega)-\kappa_n(\omega)]\overline{p}_{\ell s}^{(\infty)}(-L_r,y,\omega)\overline{p}_{\ell n}^{(\infty)}(-L_r,y,\omega)\dfrac{\overline{Y}_n(y,\omega)}{Y_n(y,\omega)}}{\sum_{s=1}^{m_r}\sum_{n=1}^{m_r}\overline{p}_{\ell s}^{(\infty)}(-L_r,y,\omega)\overline{p}_{\ell n}^{(\infty)}(-L_r,y,\omega)} \tag{46}$$

where

$$\overline{Y}_n(y,\omega)=\frac{\partial Y_n}{\partial y}(y,\omega)=\frac{1}{2}\{[\lambda_n(\omega)-\omega q]\mathrm{e}^{-\mathrm{i}\lambda_n(\omega)y}-[\lambda_n(\omega)+\omega q]\mathrm{e}^{\mathrm{i}\lambda_n(\omega)y}\} \tag{47}$$

Eq. (46) shows that the derivatives of the functions $\theta_0^{(L_r)}$ and $\theta_j^{(L_r)}$ with respect to coordinate $y$ are generally not null. Consequently, these functions as well as the function $\theta^{(L_r)}$ [Eq. (37)] are generally not constant over reservoir height. This behavior will be investigated numerically later as well as the implications of heightwise variations of TBCs on the frequency response curves of hydrodynamic pressures and forces applied at dam upstream face.

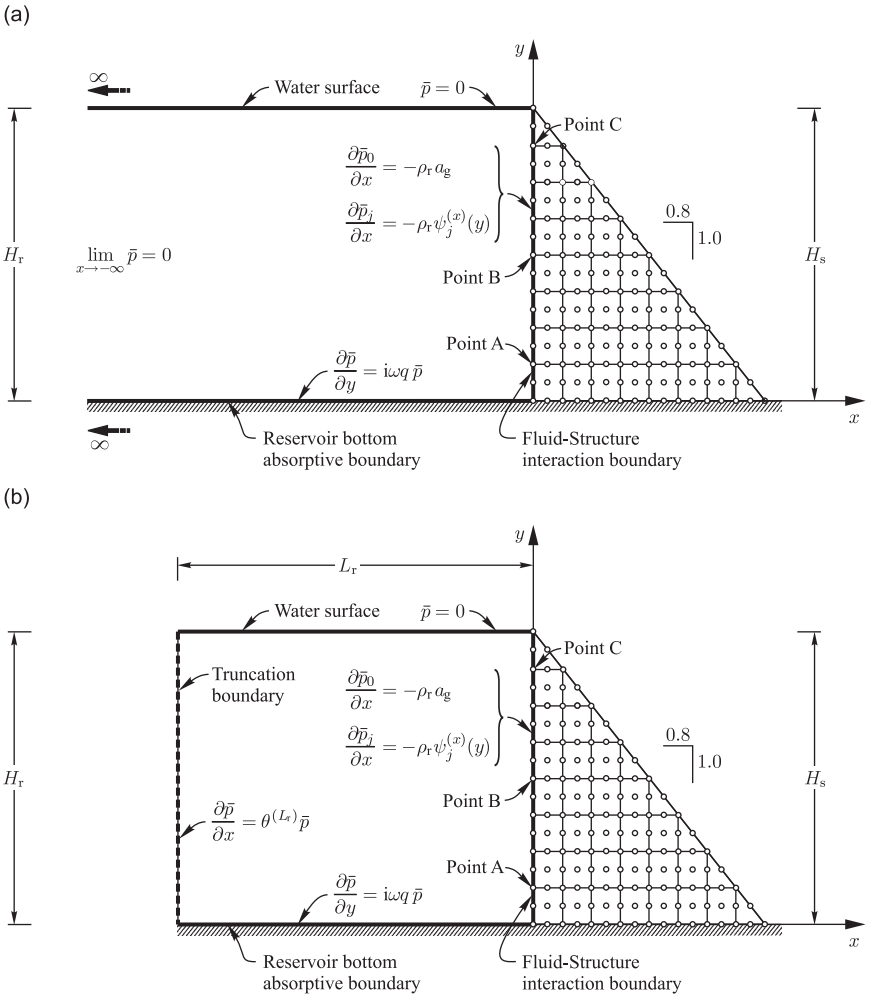


**Fig. 2.** Dam–reservoir systems studied and boundary conditions used: (a) dam impounding a semi-infinite reservoir; (b) dam impounding a truncated-length reservoir.

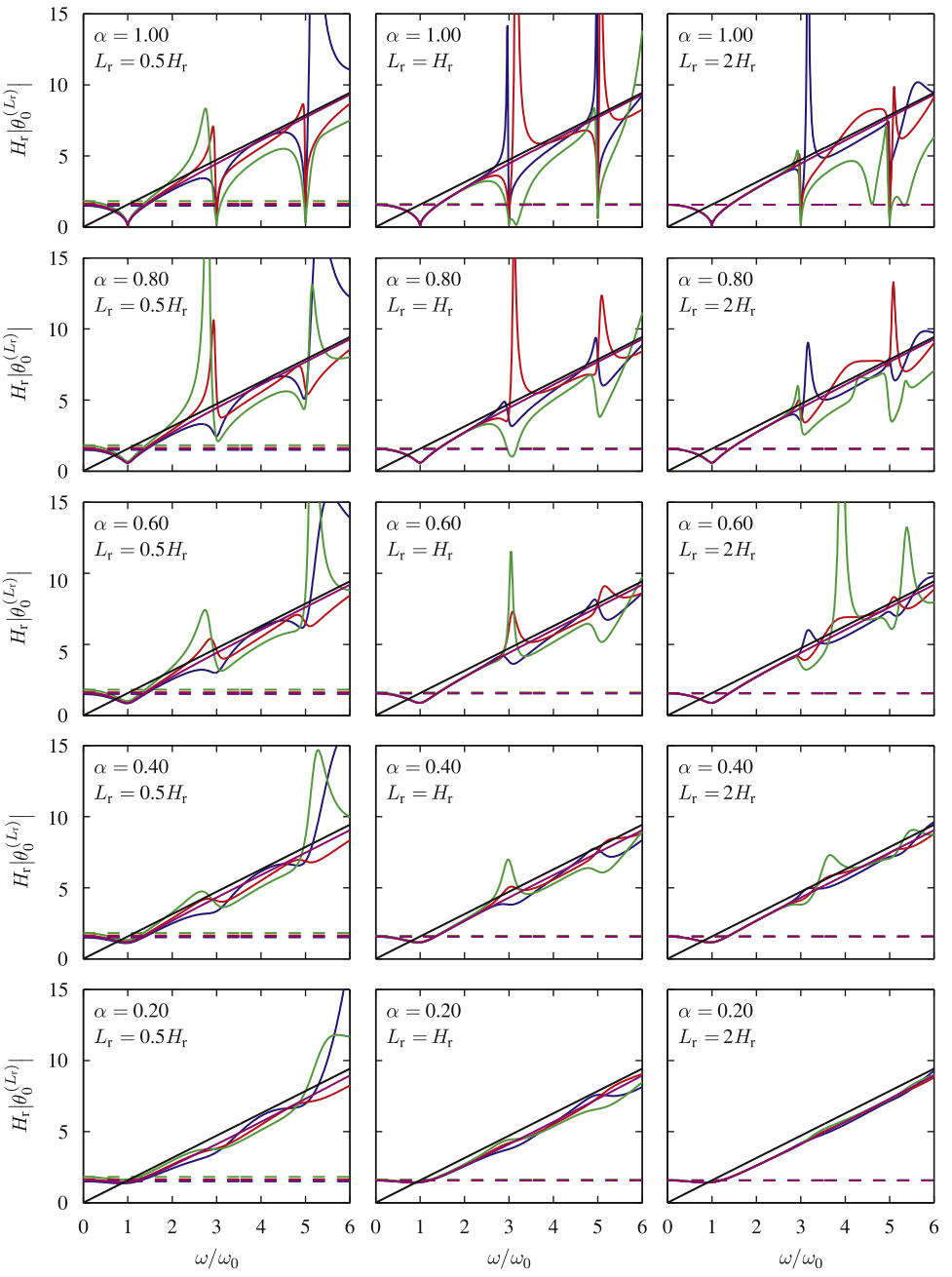


**Fig. 3.** Variation of the parameter $H_r|\theta_0^{(L_r)}|$ for a rigid dam as a function of frequency ratio $\omega/\omega_0$, height $y$, wave reflection coefficient $\alpha$ and truncation length $L_r$. —— $y_A = 0.1H_r$; —— $y_B = 0.5H_r$; —— $y_C = 0.9H_r$; ——Sommerfeld BC; ——Sharan BC. Continuous lines: compressible water; dotted lines: incompressible water.

As proven in Appendix A, if functions $\theta_\ell^{(L_r)}$ were assumed constant over reservoir height, i.e. independent of the $y$ coordinate, Eqs. (43) and (44) simplify to

$$\overline{p}_{0n}^{(L_r)}(x,y,\omega) = -2\rho_r a_g H_r \frac{\lambda_n^2(\omega)}{\beta_n(\omega)} \frac{I_{0n}(\omega)}{\kappa_n(\omega)} X_{0n}^{(L_r)}(x,\omega) Y_n(y,\omega) \tag{48}$$

$$\overline{p}_{jn}^{(L_r)}(x,y,\omega) = -2\rho_r H_r \frac{\lambda_n^2(\omega)}{\beta_n(\omega)} \frac{I_{jn}(\omega)}{\kappa_n(\omega)} X_{jn}^{(L_r)}(x,\omega) Y_n(y,\omega) \tag{49}$$

where $X_{\ell n}^{(L_r)}$ and $\zeta_{\ell n}^{(L_r)}$ are given for $\ell = 0, j$ by Eqs. (A.32) and (A.33) of Appendix A.

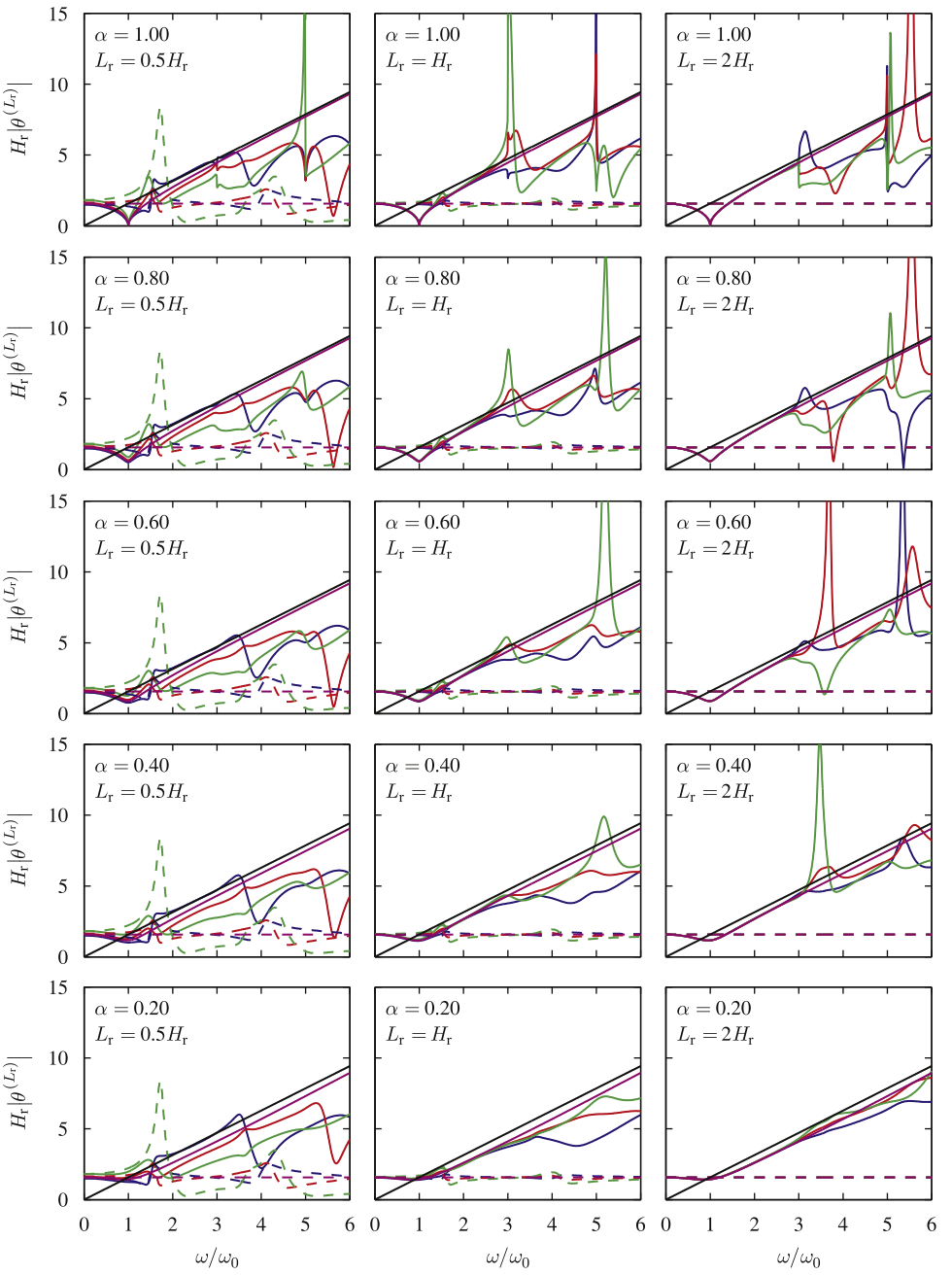


**Fig. 4.** Variation of the parameter $H_r|\theta^{(L_r)}|$ for a flexible dam $E_s = 35$ GPa as a function of frequency ratio $\omega/\omega_0$, height $y$, wave reflection coefficient $\alpha$ and truncation length $L_r$. —— $y_A = 0.1H_r$; —— $y_B = 0.5H_r$; —— $y_C = 0.9H_r$; ——Sommerfeld BC; ——Sharan BC. Continuous lines: compressible water; dotted lines: incompressible water.

For illustration purposes, Eqs. (48), (49), and then Eqs. (41) and (42) will be used later to investigate the following height-independent TBCs:

- Sommerfeld radiation boundary condition [17,18], corresponding to

$$\theta_0^{(L_r)}(\omega) = \theta_j^{(L_r)}(\omega) = \frac{i\omega}{C_r} \tag{50}$$

- Sharan boundary condition [25,26], corresponding to

$$\theta_0^{(L_r)}(\omega) = \theta_j^{(L_r)}(\omega) = \kappa_1(\omega) \tag{51}$$

We note that the Sharan boundary condition is a special case of Eq. (39) with $\tilde{m}_r = 1$.

Once hydrodynamic pressures are determined for each reservoir mode $n$, Eqs. (41) and (42) are used to sum up the contributions of the $\tilde{m}_r$ reservoir modes included in the analysis. The FRF for total hydrodynamic pressure is given by

$$\overline{p}^{(L_r)}(x,y,\omega) = \overline{p}_0^{(L_r)}(x,y,\omega) - \omega^2 \sum_{j=1}^{m_s} \overline{Z}_j^{(L_r)}(\omega)\overline{p}_j^{(L_r)}(x,y,\omega) \tag{52}$$

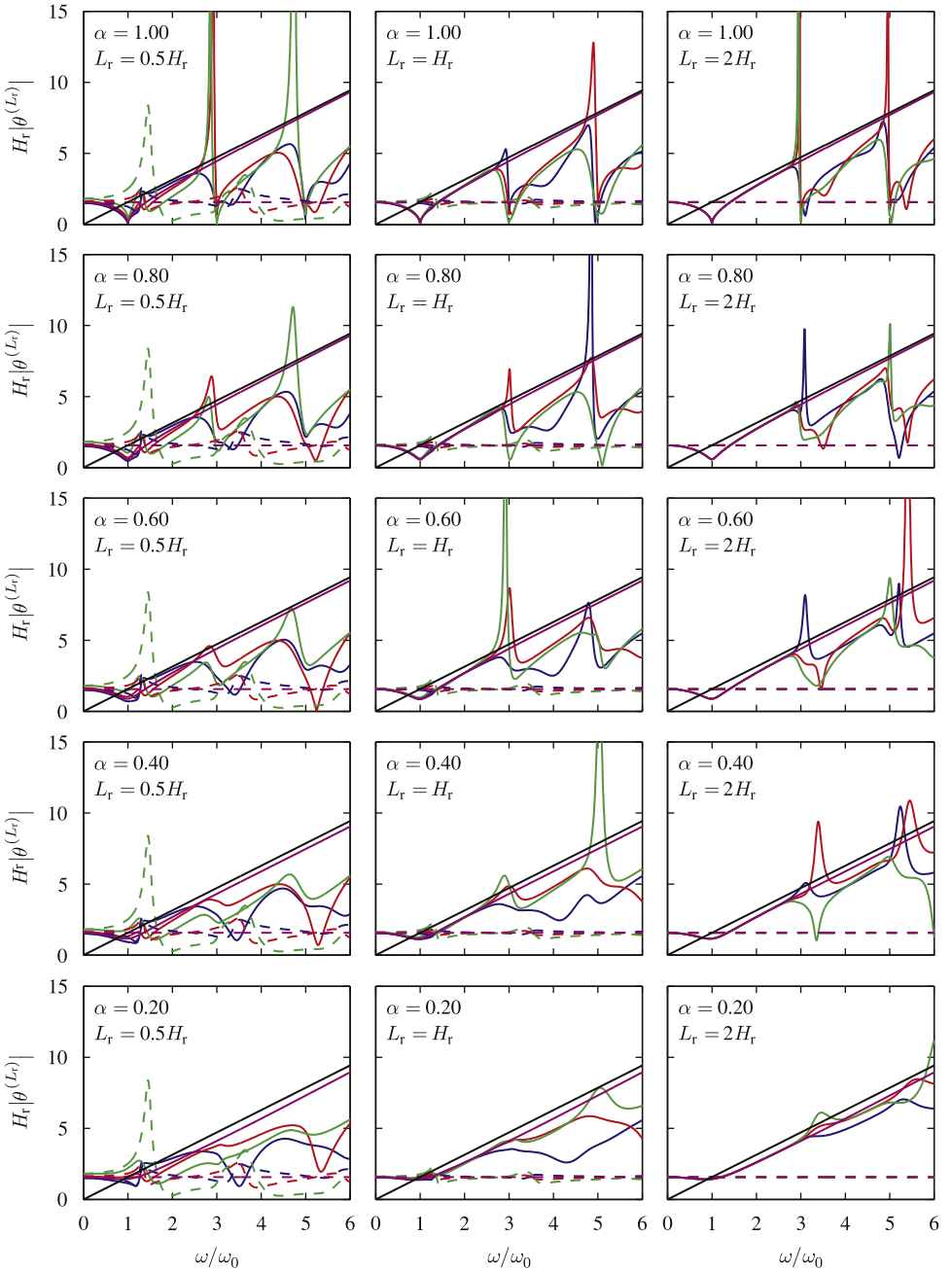


**Fig. 5.** Variation of the parameter $H_r|\theta^{(L_r)}|$ for a flexible dam $E_s = 25$ GPa as a function of frequency ratio $\omega/\omega_0$, height $y$, wave reflection coefficient $\alpha$ and truncation length $L_r$. ——$y_A = 0.1H_r$; ——$y_B = 0.5H_r$; ——$y_C = 0.9H_r$; ——Sommerfeld BC; ——Sharan BC. Continuous lines: compressible water; dotted lines: incompressible water.

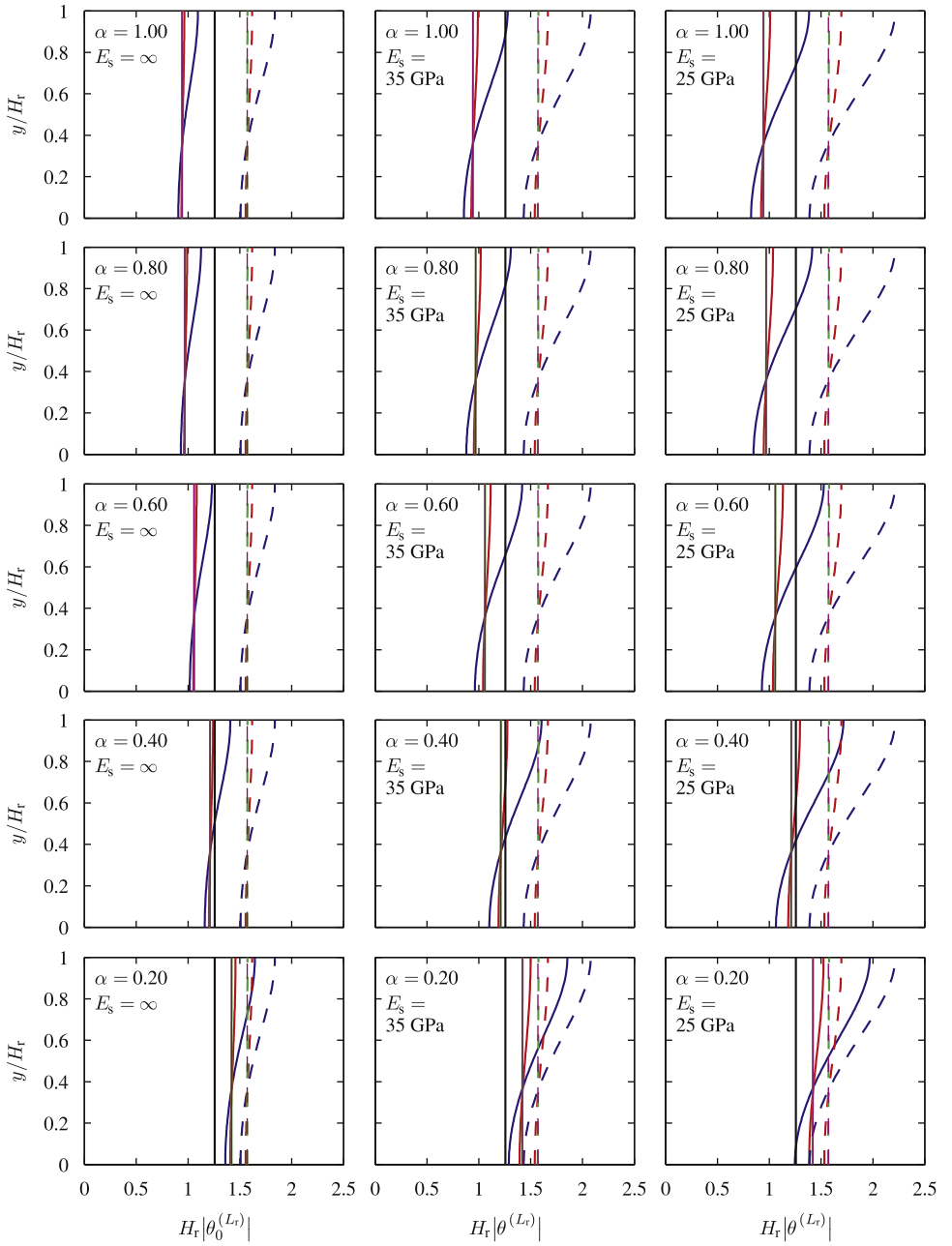


**Fig. 6.** Variation of the parameter $H_r|\theta^{(L_r)}|$ for $\omega = 0.8\omega_0$ as a function of height $y$, wave reflection coefficient $\alpha$ and truncation length $L_r$. ——$L_r = 0.5H_r$; ——$L_r = H_r$; ——$L_r = 2H_r$. ——Sommerfeld BC; ——Sharan BC. Continuous lines: compressible water; dotted lines: incompressible water.

where the vector $\overline{\mathbf{Z}}^{(L_r)}$ of generalized coordinates $\overline{Z}_j^{(L_r)}$, $j = 1 \ldots m_s$, is obtained by solving the system of equations

$$\overline{\mathbf{S}}^{(L_r)}\overline{\mathbf{Z}}^{(L_r)} = \overline{\mathbf{Q}}^{(L_r)} \tag{53}$$

in which elements of matrices $\overline{\mathbf{S}}^{(L_r)}$ and $\overline{\mathbf{Q}}^{(L_r)}$ are now defined for $n = 1 \ldots m_s$ and $j = 1 \ldots m_s$ by

$$\overline{S}_{nj}^{(L_r)}(\omega) = [-\omega^2 + (1 + \mathrm{i}\eta_s)\omega_n^2]\delta_{nj} + \omega^2 \int_0^{H_r} \overline{p}_j^{(L_r)}(0, y, \omega)\psi_n^{(x)}(y)\,\mathrm{d}y \tag{54}$$

$$\overline{Q}_n^{(L_r)}(\omega) = -a_g \boldsymbol{\psi}_n^{\mathrm{T}}\mathbf{M}\mathbf{1} + \int_0^{H_r} \overline{p}_0^{(L_r)}(0, y, \omega)\psi_n^{(x)}(y)\,\mathrm{d}y \tag{55}$$

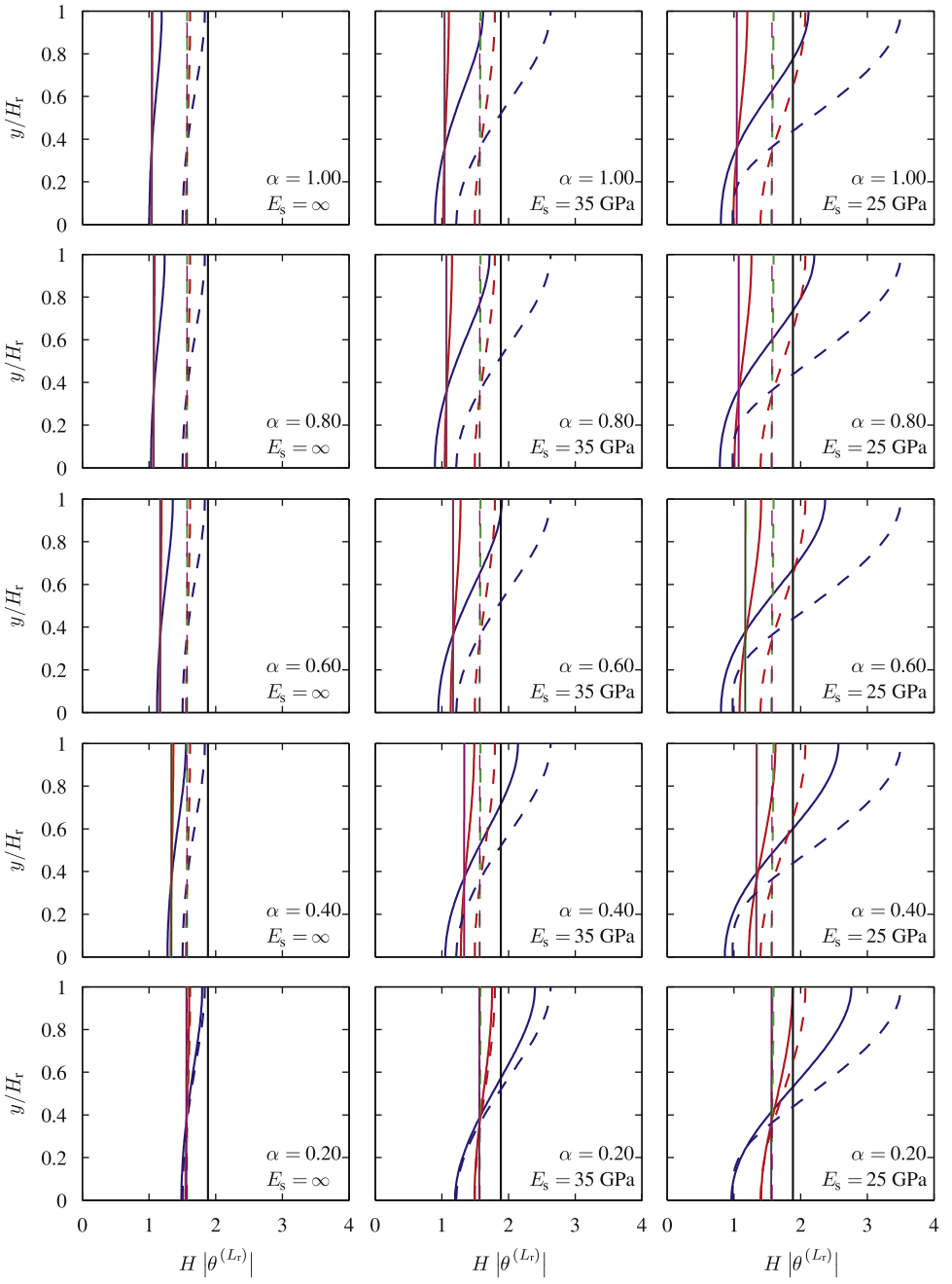


**Fig. 7.** Variation of the parameter $H_r|\theta^{(L_r)}|$ for $\omega = 1.2\omega_0$ as a function of height $y$, wave reflection coefficient $\alpha$ and truncation length $L_r$. ——$L_r = 0.5H_r$; ——$L_r = H_r$; ——$L_r = 2H_r$. ——Sommerfeld BC; ——Sharan BC. Continuous lines: compressible water; dotted lines: incompressible water.

Hydrodynamic forces at dam upstream face corresponding to hydrodynamic pressures $\overline{p}_0^{(L_r)}$ and $\overline{p}^{(L_r)}$ can then be obtained as

$$\overline{F}_0^{(L_r)}(\omega) = \int_0^{H_r} \overline{p}_0^{(L_r)}(0, y, \omega)\, \mathrm{d}y; \quad \overline{F}^{(L_r)}(\omega) = \int_0^{H_r} \overline{p}^{(L_r)}(0, y, \omega)\, \mathrm{d}y \tag{56}$$

## 3. Numerical results

### 3.1. Dam–reservoir system studied

For purpose of illustration, the new formulation presented previously is applied to analyse the dam–reservoir system shown in Fig. 2, subjected to a unit horizontal harmonic ground acceleration $\ddot{u}_g(t) = \mathrm{e}^{\mathrm{i}\omega t}$. A simplified triangular

dam cross-section with dimensions inspired from the tallest non-overflow monolith of Pine Flat dam is considered. This standard dam section was shown appropriate for a preliminary design and safety evaluation of concrete gravity dams and was introduced to develop and illustrate simplified earthquake analysis procedures proposed by Chopra et al. [2,6,41]. The dam cross-section has a height $H_s = 121.92$ m (400 ft), a downstream slope of 0.8 and a vertical upstream face. A full reservoir is assumed, i.e. $H_r = H_s$, and different reservoir truncation lengths $L_r$ are considered as will be discussed later. Fig. 2 illustrates the boundary conditions used. A dam Poisson's ratio $\nu_s = 0.2$ and mass density $\rho_s = 2400\,\mathrm{kg/m^3}$ are adopted. To assess the influence of dam stiffness, two modulus of elasticity $E_s = 25$ and 35 GPa are considered. A constant structural hysteretic damping factor $\eta_s = 0.1$ is adopted. The water is assumed compressible, with a velocity of pressure waves $C_r = 1440\,\mathrm{m/s}$ and a mass density $\rho_r = 1000\,\mathrm{kg/m^3}$. To obtain the mode shapes $\psi_j$, $j = 1 \ldots m_s$, the dam section is modeled using quadrilateral 9-node and triangular 6-node plane stress finite elements as illustrated in Fig. 2.

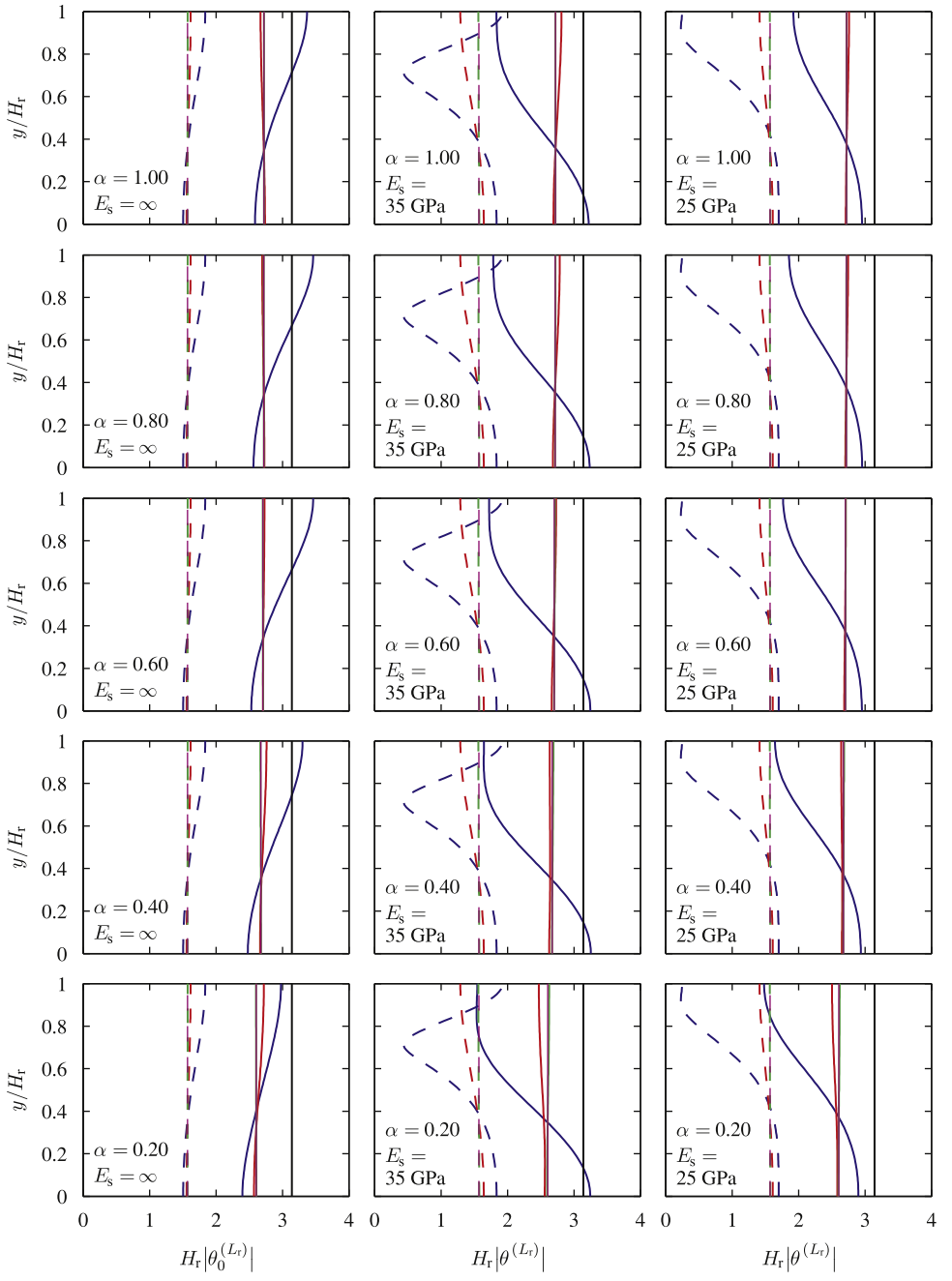


**Fig. 8.** Variation of the parameter $H_r|\theta^{(L_r)}|$ for $\omega = 2\omega_0$ as a function of height $y$, wave reflection coefficient $\alpha$ and truncation length $L_r$. ——$L_r = 0.5H_r$; ——$L_r = H_r$; ——$L_r = 2H_r$. ——Sommerfeld BC; ——Sharan BC. Continuous lines: compressible water; dotted lines: incompressible water.

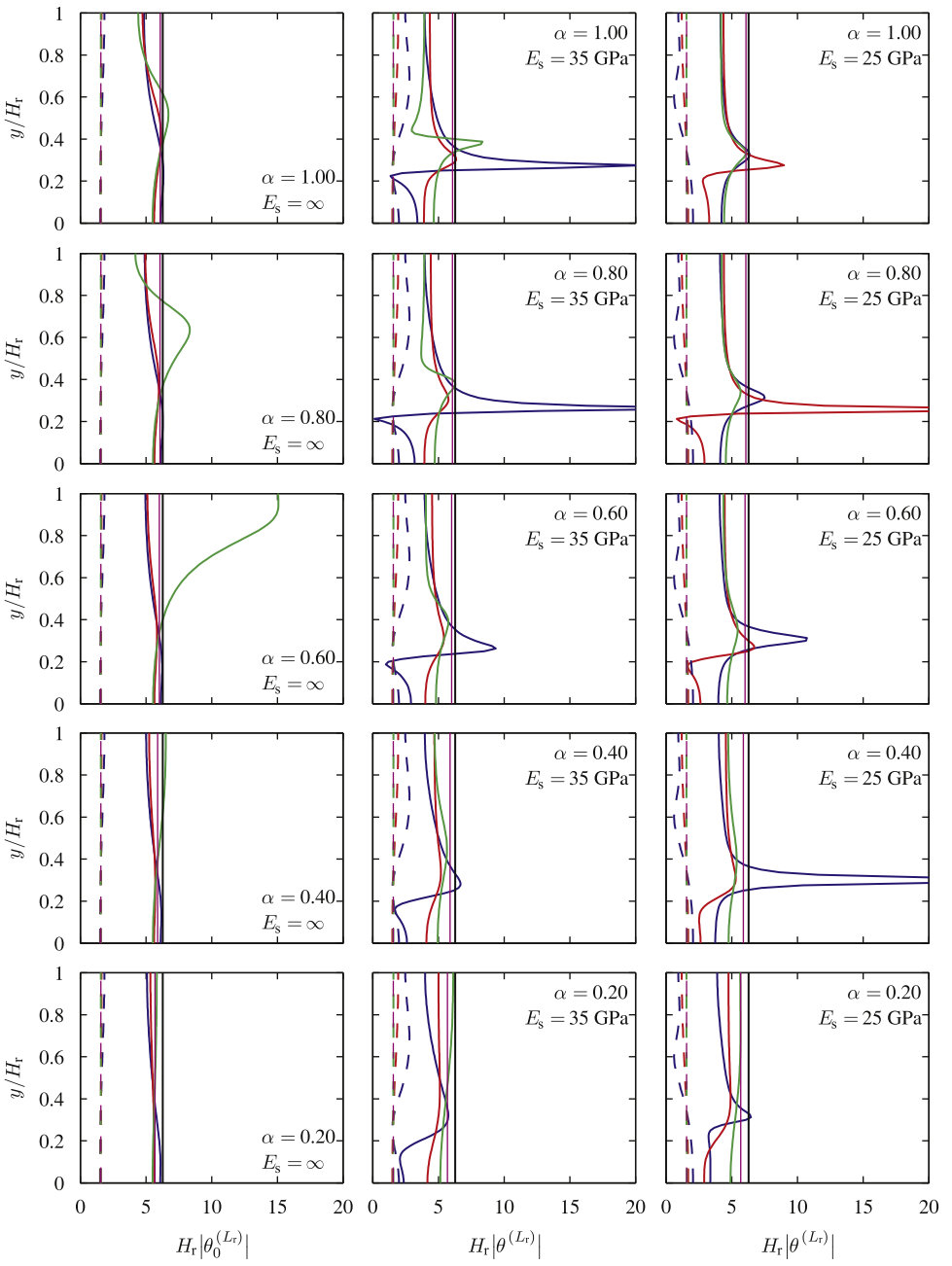


**Fig. 9.** Variation of the parameter $H_r|\theta^{(L_r)}|$ for $\omega = 4\omega_0$ as a function of height $y$, wave reflection coefficient $\alpha$ and truncation length $L_r$. ——$L_r = 0.5H_r$; ——$L_r = H_r$; ——$L_r = 2H_r$. ——Sommerfeld BC; ——Sharan BC. Continuous lines: compressible water; dotted lines: incompressible water.

### 3.2. *Investigation of the response mechanisms of various TBCs*

Before investigating the effects of various TBCs on reservoir hydrodynamic response, we first examine the dependency of the absolute values of functions $\theta_0^{(L_r)}$ and $\theta^{(L_r)}$ to frequency and reservoir depth. Fig. 3 shows the values of the dimensionless parameter $H_r|\theta_0^{(L_r)}|$ determined at three reservoir depths corresponding to points A, B and C belonging to dam–reservoir interface. Points A, B and C are located at heights $y_A = 0.1H_r$, $y_B = 0.5H_r$ and $y_C = 0.9H_r$ as shown in Fig. 2. Both compressible and incompressible water assumptions as well as Sommerfeld and Sharan boundary conditions are included. Results are determined for frequency ratios $\omega/\omega_0$ varying from 0 to 6. Three truncation lengths $L_r = 0.5H_r$, $L_r = H_r$ and $L_r = 2H_r$ and five reflection coefficients $\alpha = 1.0$, 0.8, 0.6, 0.4, and 0.2 are considered. First, it is clearly seen that the parameter $H_r|\theta_0^{(L_r)}|$ is not constant over reservoir height as usually assumed in previous research. In fact, Fig. 3 shows that this assumption holds only over a lower frequency range up to a characteristic frequency $\omega^{(L_r)}$ depending on truncation

length $L_r$. We note that $\omega^{(L_r)}$ becomes larger as truncation length increases. We also observe that the variations of $H_r|\theta_0^{(L_r)}|$ become generally smoother with increasing reservoir bottom wave absorption and truncation length, suggesting a smaller error when a TBC assumed constant over reservoir height is used in these ranges.

The results corresponding to an incompressible water assumption are obtained using Eq. (40). As expected, Fig. 3 shows that the dimensionless parameter $H_r|\theta_0^{(L_r)}|$ is not sensitive to frequency variations and reservoir bottom wave absorption. The curves are almost constant over reservoir height, namely as truncation length increases. According to Eq. (50), the Sommerfeld radiation boundary condition varies linearly with frequency ratio. For lower frequencies, i.e. in this case $\omega \leq \omega_0$, the differences between the curves representing the Sommerfeld and analytical TBC are very different, getting closer as frequency ratio increases. Fig. 3 confirms that the effectiveness of the Sommerfeld boundary condition is least for very low frequencies, and that it increases with higher frequencies, larger truncation length and more energy dissipation at reservoir bottom. The curves representing Sharan boundary condition coincide with those of the exact boundary condition

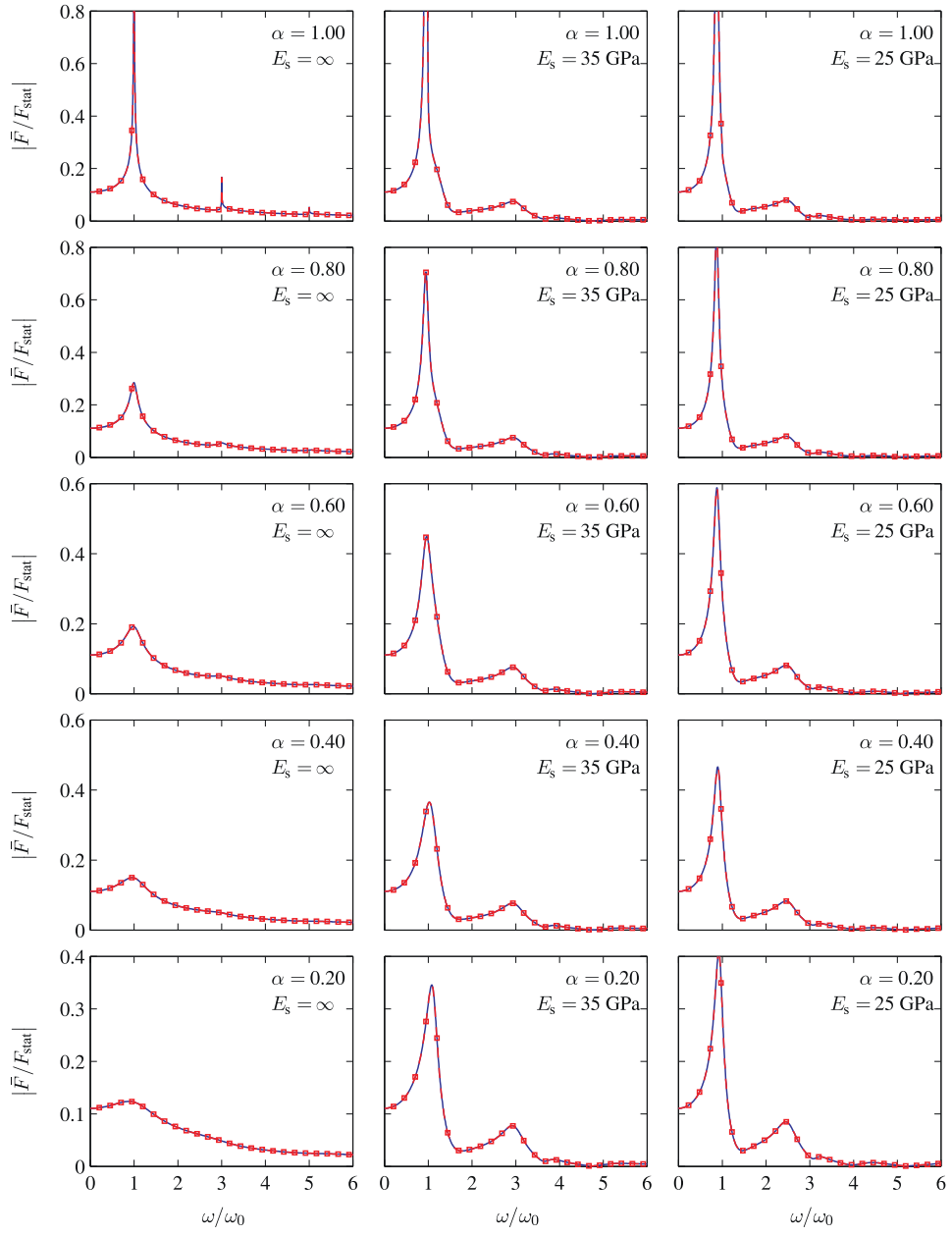


**Fig. 10.** FRFs for normalized hydrodynamic forces determined using: (i) the new formulation for a truncated reservoir ($L_r = 0.1H_r$), and (ii) the classical solution considering a semi-infinite reservoir. —□— New analytical solution; — classical solution.

up to frequency $\omega^{(L_r)}$. This behavior explains the efficiency of Sharan boundary condition in the lower frequency range as will be discussed later. We also note that the curves corresponding to Sommerfeld and Sharan boundary conditions are different at lower frequencies, while getting closer with approximately parallel curves in the higher frequency range.

The effects of dam flexibility are included next. Figs. 4 and 5 illustrate the variations of dimensionless parameter $H_r|\theta^{(L_r)}|$ considering two dam concrete modulus of elasticity $E_s = 35$ and 25 GPa, respectively. By comparing Figs. 3–5, it can be concluded that the analytical TBC is very sensitive to dam stiffness. The curves show that the amplitudes of $H_r|\theta^{(L_r)}|$ become generally sharper as dam flexibility increases. Closer examination of the curves obtained for $L_r = 0.5H_r$ shows that dam flexibility causes larger variations of the parameter $H_r|\theta^{(L_r)}|$ over reservoir height at the lower frequency range. This effect vanishes as truncation length increases. We also observe that reservoir bottom wave absorption and dam flexibility have very little effect on the maximum frequency $\omega^{(L_r)}$ below which $H_r|\theta_0^{(L_r)}|$ and $H_r|\theta_0^{(L_r)}|$ can be considered constant over

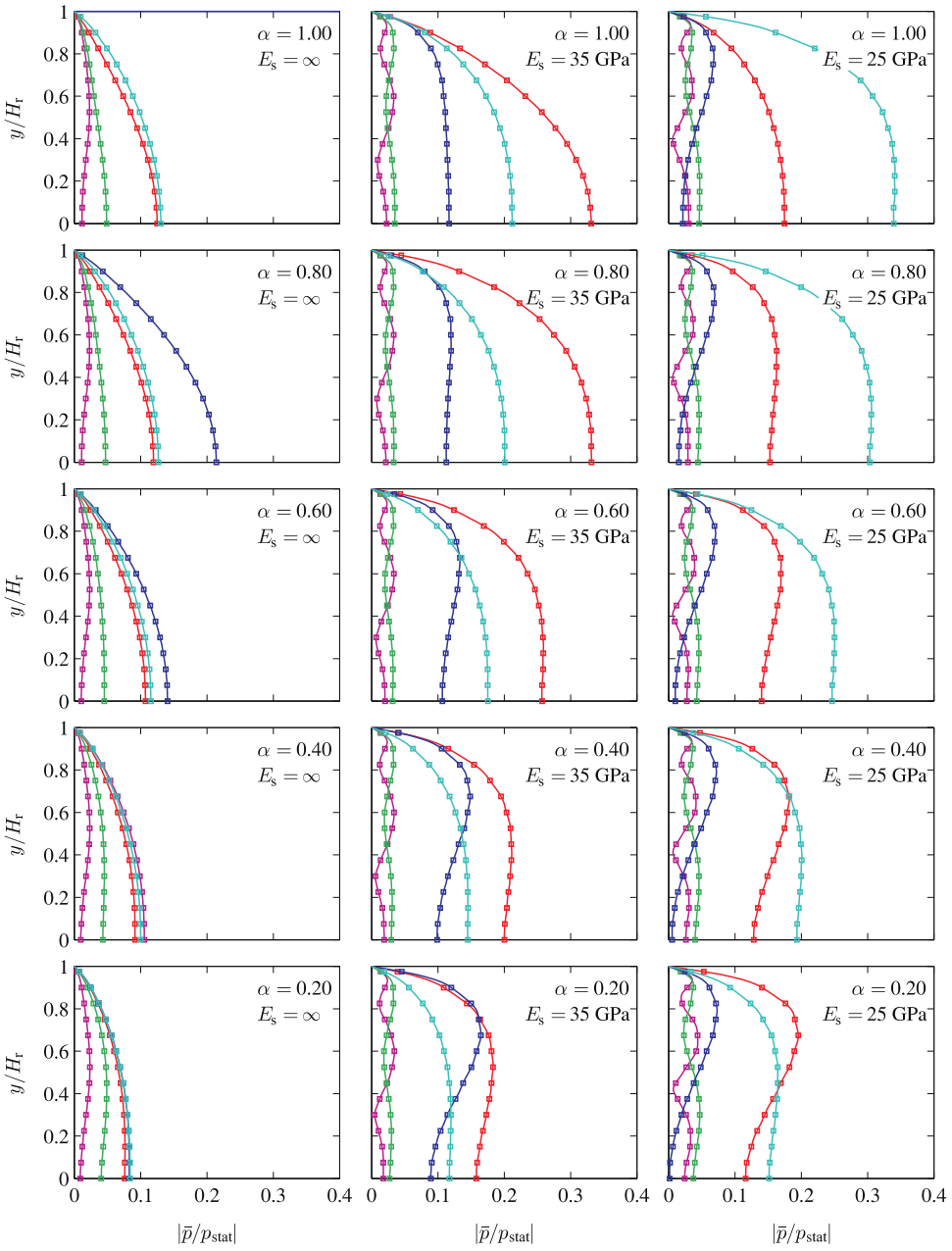


**Fig. 11.** Heightwise distributions of normalized hydrodynamic pressures on dam upstream face determined using: (i) the new formulation for a truncated reservoir ($L_r = 0.1H_r$), and (ii) the classical solution considering a semi-infinite reservoir. —□— New analytical solution; — classical solution: $\omega = 0.8\omega_0$; $\omega = \omega_0$; $\omega = 1.2\omega_0$; $\omega = 2\omega_0$; $\omega = 4\omega_0$.

reservoir height. At high frequencies, some curves exhibit sharp peaks corresponding to values of coordinate $y$ and frequency $\omega$ that make the absolute value of the denominator in Eq. (38) very small for a given truncation distance $L_r$. As observed for $H_r|\theta_0^{(L_r)}|$, increasing reservoir bottom wave absorption and truncation length cause the variations of $H_r|\theta^{(L_r)}|$ to become generally smoother. Figs. 3–5 show that the difference between the curves obtained under compressible and incompressible water assumptions is significant except for highly absorptive reservoirs at a very low frequency range. It is seen that incompressibility-based boundary conditions determined at different heights get closer as truncation length increases. We also conclude that Sharan boundary condition is in excellent agreement with the compressibility-based analytical TBC between 0 and $\omega^{(L_r)}$, and for a wider frequency range as reservoir bottom wave absorption increases.

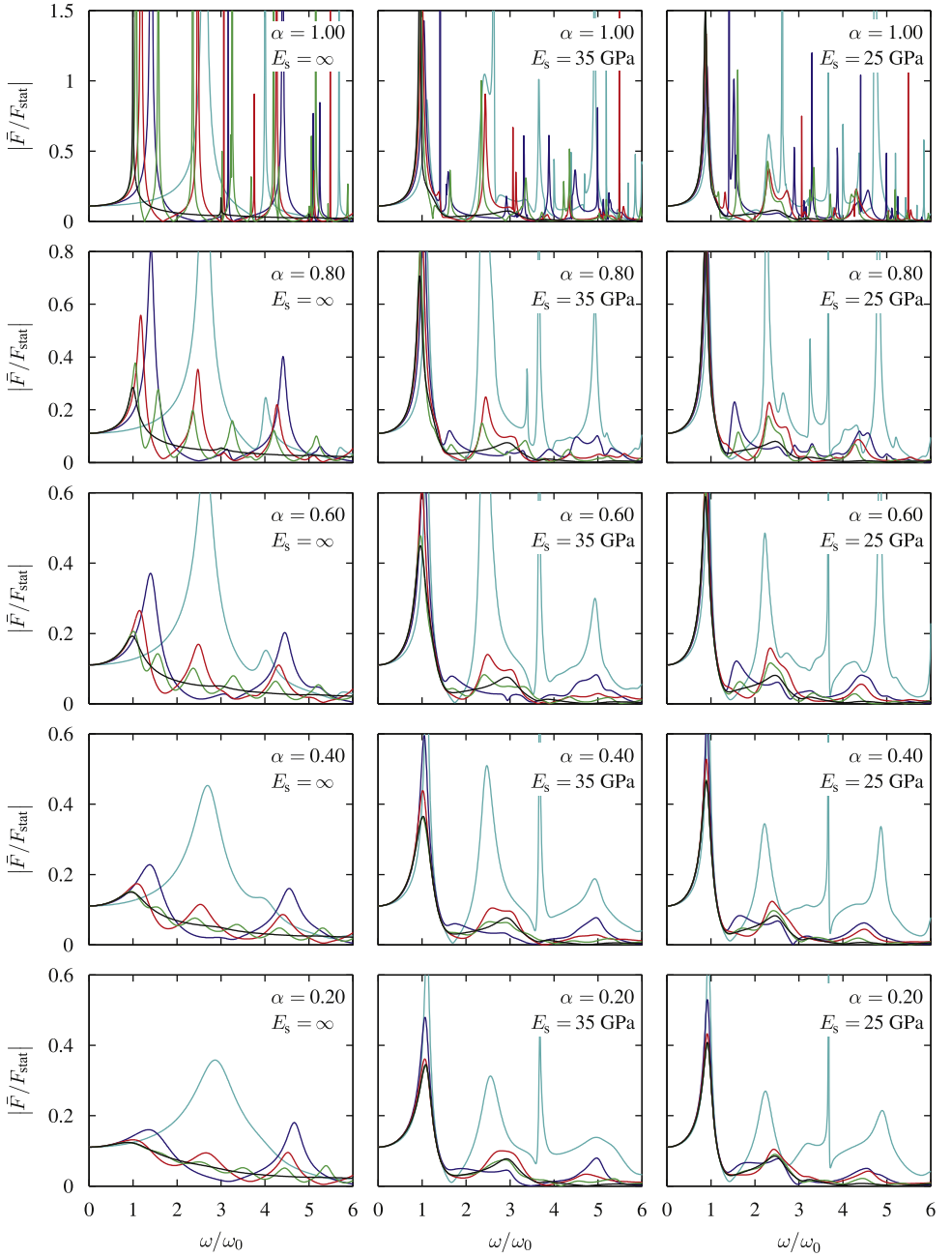


**Fig. 12.** FRFs for normalized hydrodynamic forces determined using: (i) the new analytical formulation considering an incompressibility-based analytical boundary condition, and (ii) the classical solution considering a semi-infinite reservoir. —— $L_r = 0.1H_r$; —— $L_r = 0.5H_r$; —— $L_r = H_r$; —— $L_r = 2H_r$; —— classical solution.

To further investigate the variations of $H_r|\theta_0^{(L_r)}|$ and $H_r|\theta^{(L_r)}|$ over reservoir height, the heightwise profiles of these functions are determined at three reservoir truncation lengths $L_r = 0.5H_r$, $L_r = H_r$ and $L_r = 2H_r$ and for frequencies ranging from 0 to $6\omega_0$. For brevity, only results obtained at frequency ratios $\omega/\omega_0 = 0.8$, 1.2, 2.0 and 4.0 are illustrated in Figs. 6–9, respectively. Profiles corresponding to both compressible and incompressible water assumptions as well as the constant profiles representing Sommerfeld and Sharan boundary conditions are shown. We first observe that the profiles are sensitive to dam stiffness, reservoir bottom wave absorption and frequency ratio and that they tend to become constant over reservoir height as truncation length increases. At the lower frequency ratios $\omega/\omega_0 = 0.8$ and 1.2, we observe that the compressibility-based profiles converge towards incompressibility-based ones as reservoir bottom wave absorption increases. This implies that the error associated with the use of an incompressibility-based TBC condition increases for highly reflective reservoirs. Figs. 6 and 7 also show that the three incompressibility-based profiles have each an inflexion

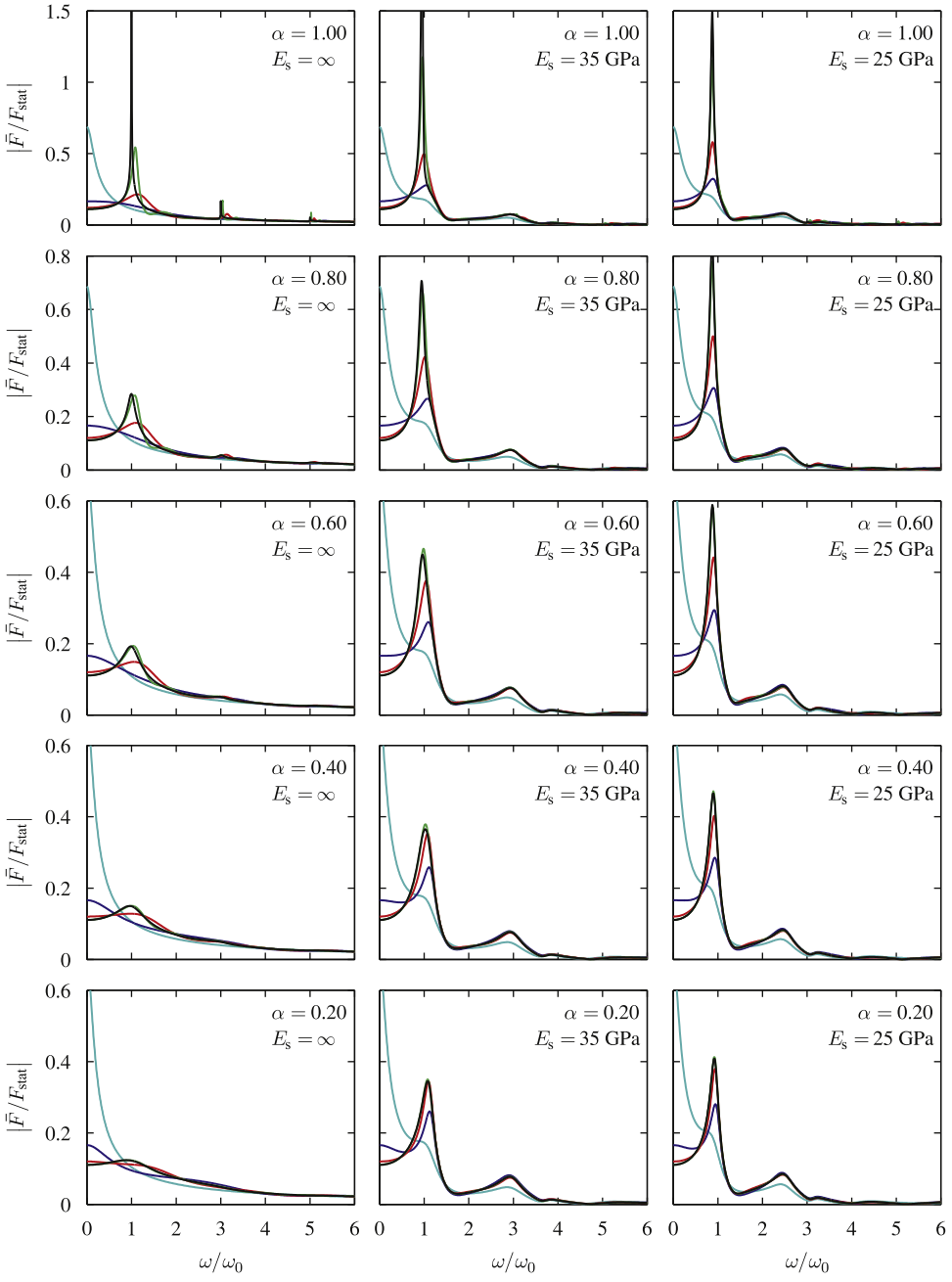


**Fig. 13.** FRFs for normalized hydrodynamic forces determined using: (i) the new analytical formulation considering Sommerfeld boundary condition, and (ii) the classical solution considering a semi-infinite reservoir. — $L_r = 0.1H_r$; — $L_r = 0.5H_r$; — $L_r = H_r$; — $L_r = 2H_r$; — classical solution.

point that is almost common. The same applies to the compressibility-based profiles. We note that the inflexion point is approximately located at the same reservoir height for all the profiles. Incompressibility- and compressibility-based Sharan boundary conditions also approximately pass through this inflexion point. A closer look at curves shows that the maximum variation of $H_r|\theta_0^{(L_r)}|$ and $H_r|\theta^{(L_r)}|$ over height increases with reservoir bottom wave absorption and dam flexibility. This behavior can be used to evaluate the error resulting from the use an incompressibility- or compressibility-based Sharan boundary condition. Figs. 8 and 9 show that, at higher frequency ratios $\omega/\omega_0 = 2.0$ and 4.0, convergence between compressibility- and incompressibility-based profiles with increasing reservoir bottom wave absorption and truncation length is not as obvious as for lower frequency ratios. Some profiles have now more that one inflexion point, i.e. the case $\alpha = 1$, $E_s = 35$ GPa and $L_r = 2H_r$, and some show sharp peaks corresponding to a very small absolute value of the denominator in Eq. (38), i.e. the case $\alpha = 0.8$, $E_s = 25$ GPa and $L_r = H_r$.

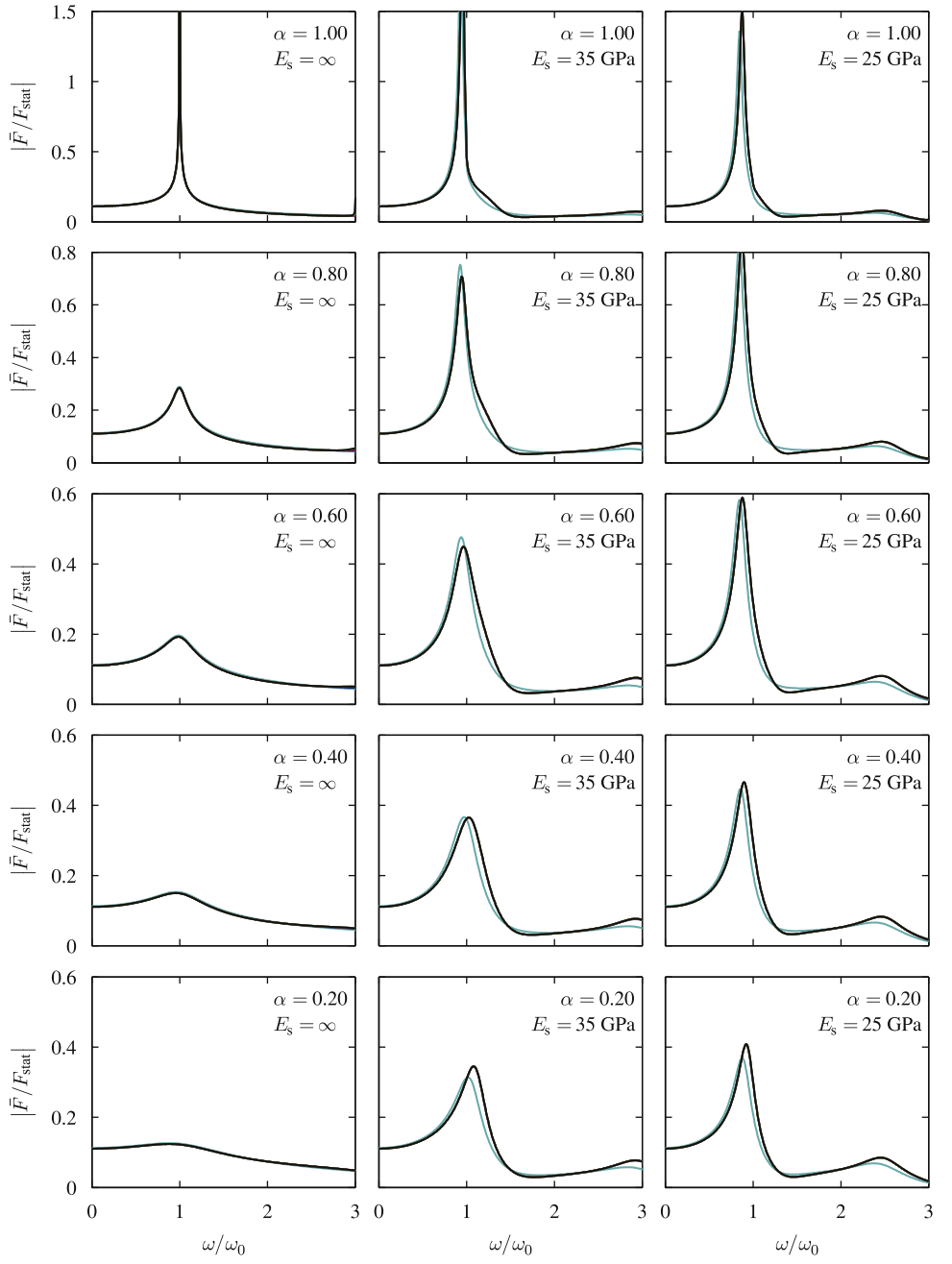


**Fig. 14.** FRFs for normalized hydrodynamic forces determined for low frequencies using: (i) the new analytical formulation considering Sharan boundary condition, and (ii) the classical solution considering a semi-infinite reservoir. —— $L_r = 0.1H_r$; —— $L_r = 0.5H_r$; —— $L_r = H_r$; —— classical solution.

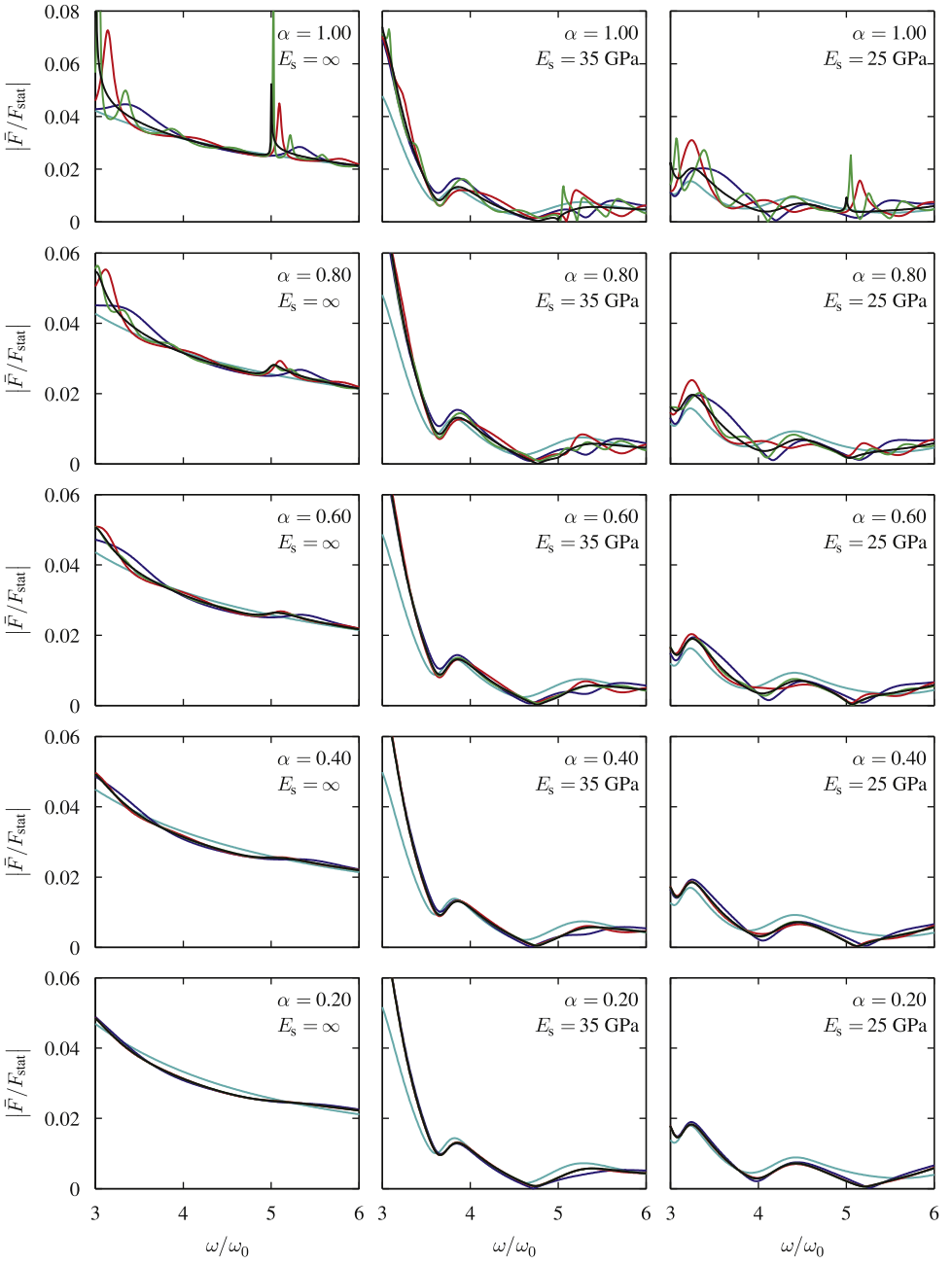


**Fig. 15.** FRFs for normalized hydrodynamic forces determined for high frequencies using: (i) the new analytical formulation considering Sharan boundary condition, and (ii) the classical solution considering a semi-infinite reservoir. —— $L_r = 0.1H_r$; —— $L_r = 0.5H_r$; —— $L_r = H_r$; —— classical solution.

### 3.3. Error analyses

The formulations presented previously were fully programmed using MATLAB® [37]. To first validate the new formulation, it is used to determine hydrodynamic forces and pressures acting on the upstream face of the dam when applying the analytical TBC at a reservoir truncation length as small as $L_r = 0.1H_r$. Rigid and flexible dams with $E_s = 35$ and 25 GPa are considered. In each case, five reflection coefficients $\alpha = 1.0$, 0.8, 0.6, 0.4, and 0.2 are investigated. Fig. 10 compares the hydrodynamic force FRFs obtained to those determined using the classical solution presented in Section 2.1, while Fig. 11 illustrates the heightwise distributions of hydrodynamic pressure determined at different frequencies using both methods. Hydrodynamic forces and pressures are normalized by hydrostatic force $F_{stat} = \rho_r g H_r^2/2$ and hydrostatic pressure $p_{stat} = \rho_r g H_r$, respectively. As can be seen, the new formulation yields a prefect agreement, irrespective of the level of reservoir bottom wave absorption and dam stiffness.

The validated new formulation is applied next to assess the effectiveness of various TBCs and determine the error associated with their use. The effect of an incompressibility-based TBC at three truncation lengths $L_r = 0.5H_r$, $L_r = H_r$ and $L_r = 2H_r$ of a compressible reservoir is investigated first. Rigid and flexible dams as well as different reservoir bottom wave absorption levels are considered. Fig. 12 shows the obtained frequency response curves of hydrodynamic forces as well as the classical solutions. The large discrepancies in the results show that incompressibility-based TBCs may induce significant errors, although better agreement is found in the lower frequency range for reservoirs with a highly absorptive bottom. The Sommerfeld radiation boundary condition presented in Eq. (50) is studied next. Using Eqs. (48), (49), and then Eqs. (41) and (42), hydrodynamic pressure FRFs of hydrodynamic forces are determined considering three reservoir truncation lengths $L_r = 0.5H_r$, $L_r = H_r$ and $L_r = 2H_r$. Fig. 13 shows the results obtained as well as the classical solutions for a semi-infinite reservoir. It is seen that the frequency response curves are very sensitive to reservoir truncation length. In the low frequency range, the Sommerfeld radiation boundary condition is indeed effective only for relatively high reservoir

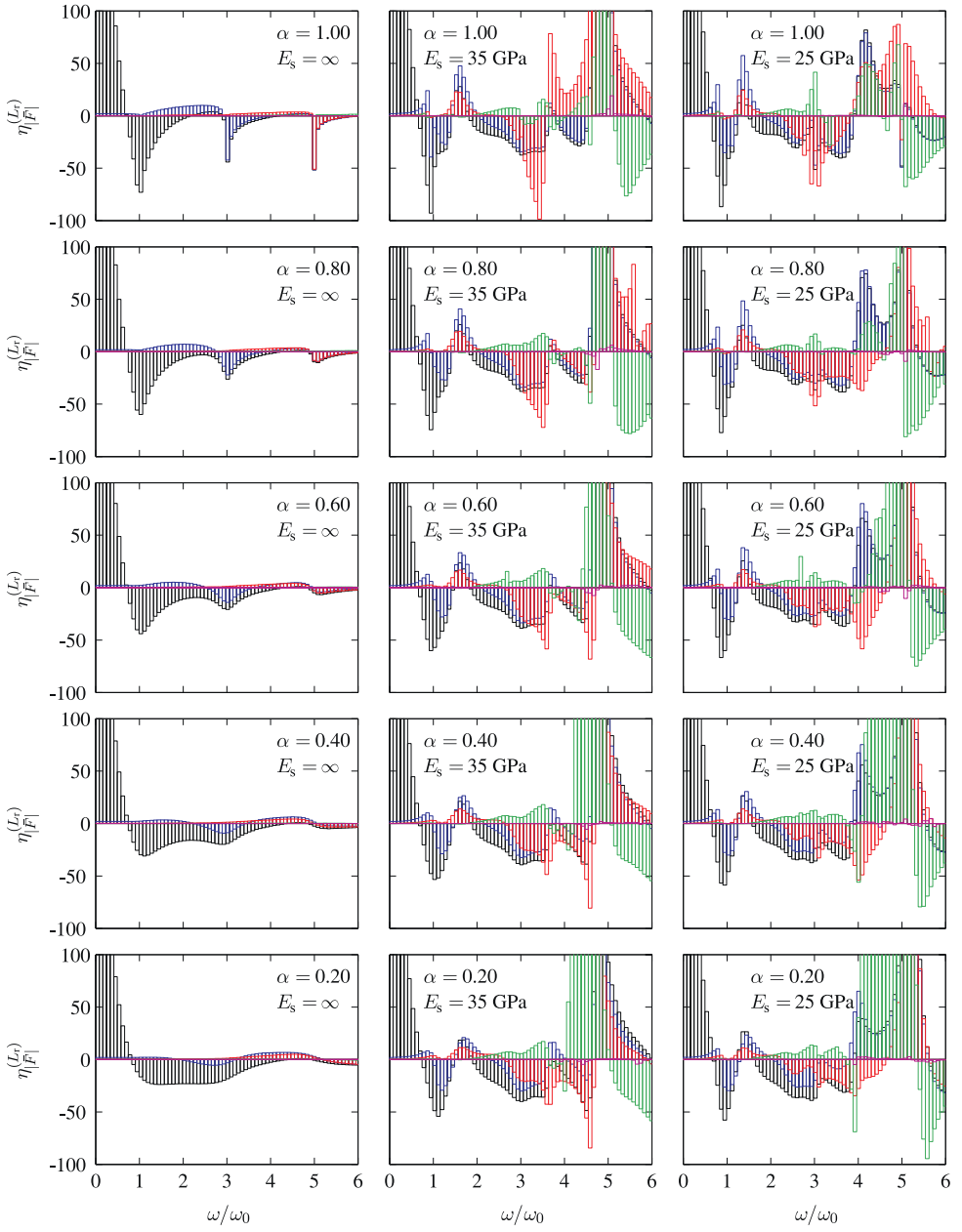


**Fig. 16.** Hydrodynamic force error estimators for a truncation length $L_r = 0.1H_r$. —— Sommerfeld BC; —— Sharan BC; —— analytical BC with $\tilde{m}_r = 2$; —— analytical BC with $\tilde{m}_r = 3$; —— analytical BC with $\tilde{m}_r = 10$.

truncation lengths, of the order of $L_r = 2H_r$ in the present case. However, even when using such an important truncation length, some discrepancies are persistent at the higher frequency range, namely for reservoirs with a highly absorptive bottom. Frequency response curves of hydrodynamic forces obtained using Sharan boundary condition [Eq. (51)] at three reservoir truncation lengths $L_r = 0.1H_r$, $L_r = 0.5H_r$ and $L_r = H_r$ are then examined. To allow clear reading of the curves, Fig. 14 illustrates the results for alow frequency range from 0 to $3\omega_0$, and Fig. 15 for a high frequency range from $3\omega_0$ to $6\omega_0$. We observe that Sharan boundary condition yields excellent results in the low frequency range for truncation lengths as small as $L_r = 0.1H_r$ for the rigid dam case. When dam flexibility is included, this truncation length yields some discrepancies with the classical solution, and a larger truncation length $L_r = 0.5H_r$ is required to reach an excellent agreement. In the higher frequency range, Fig. 15 reveals that discrepancies are induced even for truncation lengths as high as $L_r = H_r$.

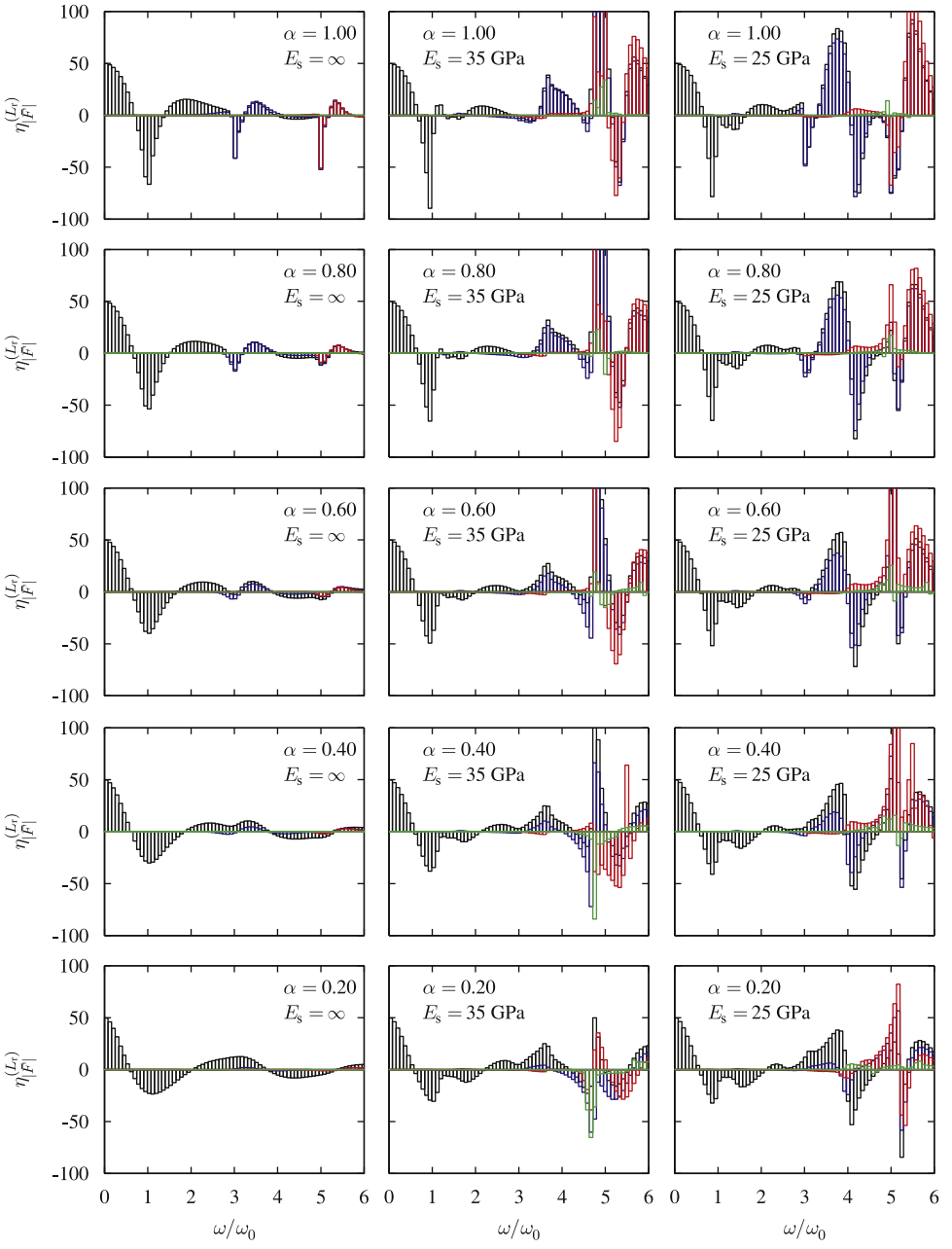


**Fig. 17.** Hydrodynamic force error estimators for a truncation length $L_r = 0.5H_r$. —— Sommerfeld BC; —— Sharan BC; —— analytical BC with $\tilde{m}_r = 2$; —— analytical BC with $\tilde{m}_r = 3$.

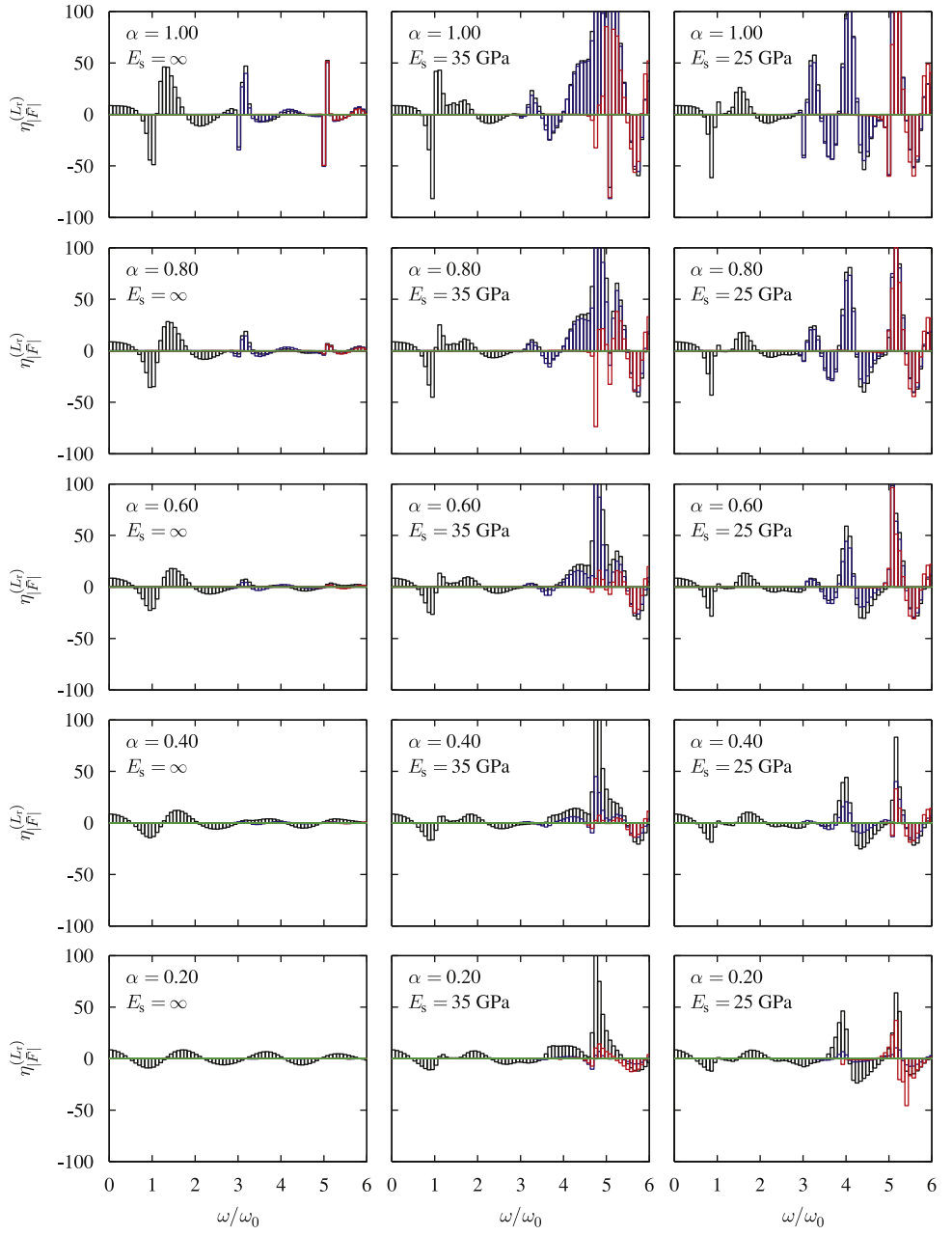


**Fig. 18.** Hydrodynamic force error estimators for a truncation length $L_r = H_r$. —— Sommerfeld BC; —— Sharan BC; —— analytical BC with $\tilde{m}_r = 2$; —— analytical BC with $\tilde{m}_r = 3$.

Accurate evaluation of hydrodynamic forces acting on a dam upstream face is of practical value for its design or safety evaluation. To get more insight into the sensitivity of hydrodynamic forces to a given TBC, the following error estimators are proposed

$$\eta^{(L_r)}_{|\overline{F}_0|}(\omega) = \frac{|\overline{F}^{(L_r)}_0(\omega)| - |\overline{F}^{(\infty)}_0(\omega)|}{|\overline{F}^{(\infty)}_0(\omega)|}; \quad \eta^{(L_r)}_{|\overline{F}|}(\omega) = \frac{|\overline{F}^{(L_r)}(\omega)| - |\overline{F}^{(\infty)}(\omega)|}{|\overline{F}^{(\infty)}(\omega)|} \tag{57}$$

Figs. 16–19 illustrate error estimators $\eta^{(L_r)}_{|\overline{F}_0|}$ and $\eta^{(L_r)}_{|\overline{F}|}$ for hydrodynamic forces determined using Sommerfeld, Sharan and truncated analytical TBCs [Eq. (39)] considering $\tilde{m}_r = 2$ to $m_r$. Results are shown for four reservoir truncation lengths $L_r = 0.1H_r$, $L_r = 0.5H_r$, $L_r = H_r$ and $L_r = 2H_r$. Error estimators are given in percent and are presented as bar charts equally spaced at frequency increments of $\Delta\omega = 0.08\omega_0$ over a frequency ratio range from 0 to 6. For each truncation length, rigid and flexible dams with $E_s = 35$ and 25 GPa are investigated, as well as five reflection coefficients $\alpha = 1.0$, 0.8, 0.6, 0.4, and

0.2. The bar charts in Fig. 16 clearly indicate that the error associated with the Sommerfeld boundary condition is the highest for most of the frequency range of interest. It is seen that the Sharan boundary condition yields satisfactory results only for very low frequencies. The error associated with the Sharan boundary condition varies significantly as a function of frequency ratio and dam flexibility, but we note that this error globally increases with dam stiffness. Sharan and Sommerfeld boundary conditions yield similar error estimators in the higher frequency range. We also observe that error estimators are less sensitive to reservoir bottom wave absorbtion. More reservoir modes need to be included to match hydrodynamic pressures in the higherfrequency range. The number of reservoir modes required for convergence in a rigid dam case, i.e. $\tilde{m}_r \approx 3$, is less than that required in the case of a flexible dam, i.e. $\tilde{m}_r \approx 10$. It is important to note, however, that an increase in the number of reservoir modes does not necessarily reduce the error estimators over the whole frequency range, but rather enlarges the lower frequency range over which error is minimum. No definite trend could be identified regarding the sign of the error estimators. For example, Sharan boundary condition is shown to be alternatively

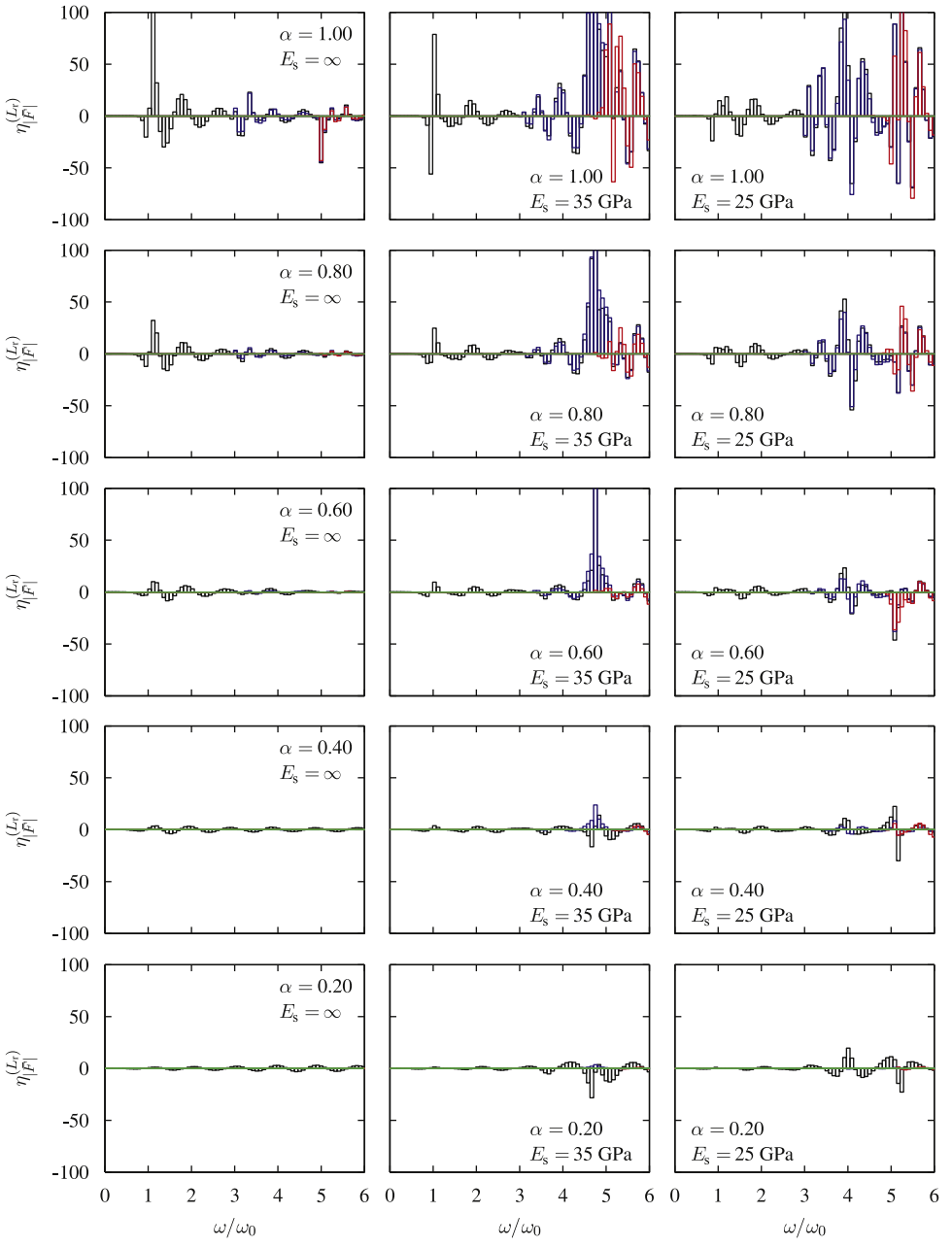


**Fig. 19.** Hydrodynamic force error estimators for a truncation length $L_r = 2H_r$. —— Sommerfeld BC; —— Sharan BC; —— analytical BC with $\tilde{m}_r = 2$; —— analytical BC with $\tilde{m}_r = 3$.

**Table 1**
Error estimation of hydrodynamic force coefficients for a gravity dam with modulus of elasticity $E_s = 25$ GPa.

| Truncation length | Boundary condition | Reservoir bottom wave absorption levels | | | | | | | | | |
|---|---|---|---|---|---|---|---|---|---|---|---|
| | | $\alpha = 1.0$ | | $\alpha = 0.8$ | | $\alpha = 0.6$ | | $\alpha = 0.4$ | | $\alpha = 0.2$ | |
| | | $\eta_{\omega_r}^{(L_r)}$ | $\eta_{c_h}^{(L_r)}$ | $\eta_{\omega_r}^{(L_r)}$ | $\eta_{c_h}^{(L_r)}$ | $\eta_{\omega_r}^{(L_r)}$ | $\eta_{c_h}^{(L_r)}$ | $\eta_{\omega_r}^{(L_r)}$ | $\eta_{c_h}^{(L_r)}$ | $\eta_{\omega_r}^{(L_r)}$ | $\eta_{c_h}^{(L_r)}$ |
| $L_r = 0.1H_r$ | Sommerfeld TBC | – | – | – | – | – | – | – | – | – | – |
| | Sharan TBC | −3.773 | −10.764 | −2.857 | −2.181 | −3.773 | −1.037 | −4.587 | −4.055 | −4.504 | −9.642 |
| | Analytical TBC, $\tilde{m}_r = 2$ | −0.943 | −0.263 | 0.000 | 2.185 | 0.000 | 2.402 | −0.917 | 2.735 | 0.000 | 2.798 |
| | Analytical TBC, $\tilde{m}_r = 3$ | 0.000 | −0.998 | 0.000 | −0.902 | 0.000 | 0.211 | −0.917 | 0.484 | 0.000 | 0.527 |
| $L_r = 0.5H_r$ | Sommerfeld TBC | 1.886 | −78.810 | 3.809 | −64.121 | 4.716 | −50.075 | 3.669 | −38.720 | 2.702 | −31.226 |
| | Sharan TBC | 0.000 | −0.341 | 0.000 | 0.034 | 0.000 | −0.005 | −0.917 | −0.103 | 0.000 | −0.301 |
| | Analytical TBC, $\tilde{m}_r = 2$ | 0.000 | −0.001 | 0.000 | 0.005 | 0.000 | 0.006 | 0.000 | 0.006 | 0.000 | 0.006 |
| | Analytical TBC, $\tilde{m}_r = 3$ | 0.000 | 0.000 | 0.000 | 0.000 | 0.000 | 0.001 | 0.000 | 0.001 | 0.000 | 0.001 |
| $L_r = 1.0H_r$ | Sommerfeld TBC | 0.943 | −61.924 | 2.857 | −41.524 | 2.830 | −25.015 | 1.834 | −13.482 | 1.801 | −7.019 |
| | Sharan TBC | 0.000 | −0.003 | 0.000 | 0.000 | 0.000 | 0.000 | 0.000 | −0.002 | 0.000 | −0.004 |
| | Analytical TBC, $\tilde{m}_r = 2$ | 0.000 | 0.000 | 0.000 | 0.000 | 0.000 | 0.000 | 0.000 | 0.000 | 0.000 | 0.000 |
| | Analytical TBC, $\tilde{m}_r = 3$ | 0.000 | 0.000 | 0.000 | 0.000 | 0.000 | 0.000 | 0.000 | 0.000 | 0.000 | 0.000 |
| $L_r = 2.0H_r$ | Sommerfeld TBC | 0.000 | −24.349 | 0.952 | −8.878 | 0.943 | −1.276 | 0.000 | 1.285 | 0.900 | 1.052 |
| | Sharan TBC | 0.000 | 0.000 | 0.000 | 0.000 | 0.000 | 0.000 | 0.000 | 0.000 | 0.000 | 0.000 |
| | Analytical TBC, $\tilde{m}_r = 2$ | 0.000 | 0.000 | 0.000 | 0.000 | 0.000 | 0.000 | 0.000 | 0.000 | 0.000 | 0.000 |
| | Analytical TBC, $\tilde{m}_r = 3$ | 0.000 | 0.000 | 0.000 | 0.000 | 0.000 | 0.000 | 0.000 | 0.000 | 0.000 | 0.000 |

conservative or non-conservative depending on the frequency ratio. As truncation length increases, Fig. 17 shows that error estimators generally diminish over the whole frequency range. For low frequencies, Sommerfeld boundary condition still yields unsatisfactory results, while the error due to Sharan boundary condition is nearly null. Fewer reservoir modes are now required to obtain convergence over all the frequency range, i.e. $\tilde{m}_r \approx 3$. The effect of energy dissipation at reservoir bottom is slightly more important than for truncation length $L_r = 0.1H_r$. It is seen that reservoir bottom wave absorption causes error estimators to slightly diminish. As previously, Sharan and Sommerfeld yield approximately similar error estimators in the higher frequency range. The same conclusions apply to Figs. 18 and 19. We namely observe that the error reduction due to reservoir bottom wave absorption becomes more predominant with increasing truncation length. For a truncation length $L_r = 2H_r$, two reservoir modes are sufficient to obtain convergence over a wide frequency range up to $\omega \approx 5\omega_0$, and three are required for higher frequencies.

Finally, predicting the first resonant frequency of a dam–reservoir system plays an important role in the assessment of the seismic response of dams. Error estimators for the first resonant frequency of a dam–reservoir system can be defined as

$$\eta_{\omega_r}^{(L_r)} = \frac{\omega_r^{(L_r)} - \omega_r^{(\infty)}}{\omega_r^{(\infty)}} \tag{58}$$

where $\omega_r^{(L_r)}$ denotes the dam–reservoir resonant frequency obtained using a truncation length $L_r$, and $\omega_r^{(\infty)}$ the resonant frequency corresponding to a semi-infinite reservoir. We may also examine error estimators for hydrodynamic force coefficients at dam upstream face

$$\eta_{c_h}^{(L_r)} = \frac{c_h^{(L_r)} - c_h^{(\infty)}}{c_h^{(\infty)}} \tag{59}$$

where hydrodynamic force coefficients $c_h^{(\infty)}$ and $c_h^{(L_r)}$ are defined by

$$c_h^{(\infty)} = \frac{|\overline{F}^{(\infty)}(\omega)|_{\max}}{F_{\text{stat}}}; \quad c_h^{(L_r)} = \frac{|\overline{F}^{(L_r)}(\omega)|_{\max}}{F_{\text{stat}}} \tag{60}$$

For purpose of illustration, error estimators determined according to Eqs. (58)–(60) are presented in Table 1 for a gravity dam with modulus of elasticity $E_s = 25$ GPa. As can be seen in this case, Sommerfeld boundary condition cannot be used to determine the first resonant frequency of the dam–reservoir system, neither the corresponding hydrodynamic force coefficient for a short truncation length $L_r = 0.1H_r$. As truncation length increases, Sommerfeld boundary condition becomes more accurate to predict the first resonant frequency. Predictions of corresponding resonant amplitudes are, however, generally less accurate, but are improved for reservoirs with a highly absorptive bottom. Sharan boundary condition yields satisfactory predictions of both first resonant frequency and corresponding amplitude, except for the short truncation length $L_r = 0.1H_r$. We also note that including additional reservoir modes, i.e. $\tilde{m}_r = 2$ to $\tilde{m}_r = 3$, yields an excellent agreement with the classical solution even for short truncation lengths and irrespective of reservoir bottom wave absorption levels.

## 4. Concluding remarks

This paper presented and validated an original formulation to study dynamically excited dam–reservoir systems with upstream TBCs. First, a review of main developments related to the application of TBCs in dam engineering was presented. Then, the detailed mathematical derivations were provided for various TBCs and their sensitivity to: (i) truncation length, (ii) reservoir depth, (iii) reservoir bottom wave absorption, (v) water compressibility, and (iv) dam stiffness was thoroughly investigated over a wide frequency range of interest in dam engineering applications. The systems of equations resulting from the analytical formulation were solved numerically to assess the accuracy and effectiveness of some classical approximate TBCs and determine the exact error associated with their use independently of FEM or BEM modeling of the reservoir. Exact analytical TBCs were also developed for comparison purposes. The effects of reservoir truncation length, reservoir bottom wave absorption, water compressibility and dam stiffness on the frequency response of hydrodynamic pressures and forces applied at a dam upstream face were identified and discussed. We showed that the widely used assumption that TBCs are height-independent holds only over a low frequency range up to a characteristic frequency which increases with truncation length. This height-dependence was observed to generally increase with higher reservoir bottom wave reflection and dam flexibility. We also concluded that the effect of water compressibility is significant except for highly absorptive reservoirs at a very low frequency range. Using the new formulation, error estimators were determined to provide guidelines for selecting TBCs to be implemented in finite element or boundary element models of dam–reservoir systems. For that purpose, the sensitivity of hydrodynamic forces acting on dam upstream face and that of the first resonant frequency of the dam–reservoir system to the various aforementioned parameters were systematically investigated. The following main trends could be identified especially when short reservoir truncation lengths are required to reduce computational burden: (i) incompressibility-based TBCs generally induce significant errors and should not be used, (ii) Sommerfeld TBC fails in predicting the first resonant frequency of the dam–reservoir system as well as hydrodynamic forces on most of the frequency range of interest, (iii) improved results can be obtained by using the Sharan TBC or the truncated analytical TBCs introduced in the paper, and applying the error estimators proposed to control the quality of the solution as a function of frequency ratio, dam flexibility and wave absorption at reservoir bottom. The in-depth parametric studies presented illustrate how the proposed formulation and error estimators can be used efficiently for a rigorous assessment of the accuracy and effectiveness of classical or newly developed TBCs, namely by defining reservoir length to depth ratios and frequency ranges for which the application of these TBCs would be recommended. We note that the proposed method, which can be easily programmed, is valuable in testing, validating or developing TBCs that are either height-dependent or independent, and frequency-dependent or independent, with the latter case being generally more suited for time domain analyses. Finally, although the paper provided the formulation and fundamental mechanisms involved in vibrating dam–reservoir systems with upstream TBCs, the methodology and findings described can be extended to other similar fluid–structure problems.

## Acknowledgments

The authors would like to acknowledge the financial support of the Natural Sciences and Engineering Research Council of Canada (NSERC).

## Appendix A

The hydrodynamic pressure frequency response functions $\overline{p}_0^{(L_r)}$ and $\overline{p}_j^{(L_r)}$ are determined in this appendix for the TBCs given by Eqs. (32) and (33). For clarity and brevity, the following notation is used in this appendix: and

$$\overline{p}_\ell^{(L_r)}(x,y,\omega)=\begin{cases}\overline{p}_0^{(L_r)}(x,y,\omega) & \text{if } \ell=0 \quad (A.1)\\ \overline{p}_j^{(L_r)}(x,y,\omega) & \text{if } \ell=j \quad (A.2)\end{cases}$$

$$f_0(y)=a_g;\quad \eta_0=a_g \tag{A.3}$$

$$f_1(y)=\psi_j^{(x)}(y);\quad \eta_1=1 \tag{A.4}$$

Throughout the appendix, subscript $\ell$ can take the values 0 or $j$.

Using the technique of separation of variables, hydrodynamic pressures can be expressed as

$$\overline{p}_\ell^{(L_r)}(x,y,\omega)=\overline{p}_{\ell x}^{(L_r)}(x,\omega)\overline{p}_{\ell y}^{(L_r)}(y,\omega) \tag{A.5}$$

Substitution into Eq. (3) yields the two differential equations

$$\frac{\mathrm{d}^2\overline{p}_{\ell x}^{(L_r)}}{\mathrm{d}x^2}-\kappa^2\overline{p}_{\ell x}^{(L_r)}=0 \tag{A.6}$$

$$\frac{d^2\overline{p}_{\ell y}^{(L_r)}}{dy^2}+\lambda^2\overline{p}_{\ell y}^{(L_r)}=0 \tag{A.7}$$

where $\lambda$ and $\kappa$ are complex constants related by

$$\kappa^2=\lambda^2-\frac{\omega^2}{C^2} \tag{A.8}$$

The general solutions of Eqs. (A.7) and (A.6) can be written, respectively, as

$$\overline{p}_{\ell x}^{(L_r)}(x,\omega)=\gamma_1^{(\ell)}(\omega)e^{-\kappa x}+\gamma_2^{(\ell)}(\omega)e^{\kappa x} \tag{A.9}$$

$$\overline{p}_{\ell y}^{(L_r)}(y,\omega)=\gamma_3^{(\ell)}(\omega)e^{-i\lambda y}+\gamma_4^{(\ell)}(\omega)e^{i\lambda y} \tag{A.10}$$

where the coefficients $\gamma_1^{(\ell)}(\omega)$, $\gamma_2^{(\ell)}(\omega)$, $\gamma_3^{(\ell)}(\omega)$ and $\gamma_4^{(\ell)}(\omega)$ are to be determined by imposing the boundary conditions.

Using the transformations of Eq. (A.5) into Eqs. (9) and (10), we obtain the boundary conditions to be satisfied by $\overline{p}_{\ell y}^{(L_r)}$

$$\frac{d\overline{p}_{\ell y}^{(L_r)}}{dy}(0,\omega)=i\omega q\overline{p}_{\ell y}^{(L_r)}(0,\omega) \tag{A.11}$$

$$\overline{p}_{\ell y}^{(L_r)}(H_r,\omega)=0 \tag{A.12}$$

Substituting $\overline{p}_{\ell y}^{(L_r)}(y,\omega)$ by its expression in Eq. (A.10) into Eqs. (A.11) and (A.12) yields Eq. (18) to be satisfied by the eigenvalues $\lambda_n(\omega)$. The associated eigenvectors $Y_n, n=1\ldots m_r$ are given by Eq. (19) and they satisfy the orthogonality relations

$$\int_0^{H_r} Y_s(y,\omega)Y_n(y,\omega)\,dy=\begin{cases}0 & \text{if } s\neq n \quad (A.13)\\ \dfrac{\beta_n(\omega)}{2\lambda_n^2(\omega)} & \text{if } s=n \quad (A.14)\end{cases}$$

Using Eq. (A.9), the hydrodynamic pressure can be expressed as the summation

$$\overline{p}_{\ell}^{(L_r)}(x,y,\omega)=\sum_{n=1}^{\infty}[\gamma_{1,n}^{(\ell)}(\omega)e^{-\kappa_n(\omega)x}+\gamma_{2,n}^{(\ell)}(\omega)e^{\kappa_n(\omega)x}]Y_n(y,\omega)\approx\sum_{n=1}^{m_r}[\gamma_{1,n}^{(\ell)}(\omega)e^{-\kappa_n(\omega)x}+\gamma_{2,n}^{(\ell)}(\omega)e^{\kappa_n(\omega)x}]Y_n(y,\omega) \tag{A.15}$$

where the complex coefficients $\kappa_n(\omega)$ are given by Eq. (20) and $m_r$ is the number of reservoir modes.

Coefficients $\gamma_{1,n}^{(\ell)}(\omega)$ and $\gamma_{2,n}^{(\ell)}(\omega)$ are to be determined by imposing the boundary conditions at dam upstream face [Eqs. (8)] and at the reservoir truncation boundary [Eqs. (32) and 33]

$$\frac{\partial\overline{p}_{\ell}^{L_r}}{\partial x}(0,y,\omega)=-\rho_r f_\ell(y) \tag{A.16}$$

$$\frac{\partial\overline{p}_{\ell}^{(L_r)}}{\partial x}(-L_r,y,\omega)=\theta_{\ell}^{(L_r)}(y,\omega)\overline{p}_{\ell}^{(L_r)}(-L_r,y,\omega) \tag{A.17}$$

which yields after substitution of Eq. (A.15)

$$\sum_{n=1}^{m_r}\kappa_n(\omega)[\gamma_{1,n}^{(\ell)}(\omega)-\gamma_{2,n}^{(\ell)}(\omega)]Y_n(y,\omega)=\rho_r f_\ell(y) \tag{A.18}$$

$$\sum_{n=1}^{m_r}\{\gamma_{1,n}^{(\ell)}(\omega)[\kappa_n(\omega)+\theta_{\ell}^{(L_r)}(y,\omega)]e^{\kappa_n(\omega)L_r}-\gamma_{2,n}^{(\ell)}(\omega)[\kappa_n(\omega)-\theta_{\ell}^{(L_r)}(y,\omega)]e^{-\kappa_n(\omega)L_r}\}Y_n(y,\omega)=0 \tag{A.19}$$

Multiplying Eq. (A.18) by eigenvectors $Y_s(y,\omega), s=1\ldots m_r$, integrating over reservoir height $H_r$ and using the orthogonality relationships in Eqs. (A.13) and (A.14) gives

$$\gamma_{2,n}^{(\ell)}(\omega)=\gamma_{1,n}^{(\ell)}(\omega)-2\rho_r\eta_\ell H_r\frac{\lambda_n^2(\omega)}{\beta_n(\omega)}\frac{I_{\ell n}(\omega)}{\kappa_n(\omega)} \tag{A.20}$$

Replacing into Eq. (A.19) yields

$$\sum_{n=1}^{m_r}\{\kappa_n[e^{-\kappa_n(\omega)L_r}-e^{\kappa_n(\omega)L_r}]-[e^{-\kappa_n(\omega)L_r}+e^{\kappa_n(\omega)L_r}]\theta_{\ell}^{(L_r)}(y,\omega)\}Y_n(y,\omega)\gamma_{1,n}^{(\ell)}(\omega)$$
$$=2\rho_r\eta_\ell H_r\sum_{n=1}^{m_r}\frac{\lambda_n^2(\omega)}{\beta_n(\omega)}\frac{I_{\ell n}(\omega)}{\kappa_n(\omega)}e^{-\kappa_n(\omega)L_r}[\kappa_n(\omega)-\theta_{\ell}^{(L_r)}(y,\omega)]Y_n(y,\omega) \tag{A.21}$$

Both sides of this equation can then be multiplied by eigenvectors $Y_s(y,\omega), s=1\ldots m_r$, and integrated over reservoir height $H_r$ to obtain the system of linear equations

$$\mathbf{A}^{(\ell)}\boldsymbol{\Gamma}^{(\ell)}=\mathbf{B}^{(\ell)} \tag{A.22}$$

in which the elements of matrix $\mathbf{A}^{(\ell)}$ and vectors $\boldsymbol{\Gamma}^{(\ell)}$ and $\mathbf{B}^{(\ell)}$ are defined for $n=1\ldots m_r$ and $s=1\ldots m_r$ as

$$\Gamma_n^{(\ell)}=\gamma_{1,n}^{(\ell)}(\omega), \tag{A.23}$$

$$A_{sn}^{(\ell)}(\omega)=\frac{\kappa_n(\omega)\beta_n(\omega)}{2\lambda_n^2(\omega)}[e^{-\kappa_n(\omega)L_r}-e^{\kappa_n(\omega)L_r}]\delta_{sn}-[e^{-\kappa_n(\omega)L_r}+e^{\kappa_n(\omega)L_r}]\int_0^{H_r}\theta_\ell^{(L_r)}(y,\omega)Y_s(y,\omega)Y_n(y,\omega)\,dy \tag{A.24}$$

$$B_s^{(\ell)}(\omega)=2\rho_r\eta_\ell H_r\sum_{n=1}^{m_r}\frac{\lambda_n^2(\omega)}{\beta_n(\omega)}\frac{I_{\ell n}(\omega)}{\kappa_n(\omega)}g\left[\frac{\kappa_n(\omega)\beta_n(\omega)}{2\lambda_n^2(\omega)}\delta_{sn}-\int_0^{H_r}\theta_\ell^{(L_r)}(y,\omega)Y_s(y,\omega)Y_n(y,\omega)\,dy\right]e^{-\kappa_n(\omega)L_r} \tag{A.25}$$

where $\delta$ is the Kronecker symbol. Eq. (A.15) transforms then to

$$\begin{aligned}\overline{p}_\ell^{(L_r)}(x,y,\omega)=&\sum_{n=1}^{m_r}\left\{[e^{-\kappa_n(\omega)x}+e^{\kappa_n(\omega)x}]\Gamma_n^{(\ell)}(\omega)-2\rho_r\eta_\ell H_r\frac{\lambda_n^2(\omega)}{\beta_n(\omega)}\frac{I_{\ell n}(\omega)}{\kappa_n(\omega)}e^{\kappa_n(\omega)x}\right\}Y_n(y,\omega)=\overline{p}_\ell^{(\infty)}(x,y,\omega)\\&+\sum_{n=1}^{m_r}[e^{-\kappa_n(\omega)x}+e^{\kappa_n(\omega)x}]\Gamma_n^{(\ell)}(\omega)Y_n(y,\omega)\end{aligned} \tag{A.26}$$

If the functions $\theta_\ell^{(L_r)}$ were assumed constant over reservoir height, i.e. independent of the $y$ coordinate, the integrals in Eqs. (A.24) and (A.25) become by virtue of orthogonality relations of eigenvectors $Y_n$:

$$\int_0^{H_r}\theta_\ell^{(L_r)}(\omega)Y_s(y,\omega)Y_n(y,\omega)\,dy=\frac{\beta_n(\omega)}{2\lambda_n^2(\omega)}\theta_\ell^{(L_r)}(\omega)\delta_{sn} \tag{A.27}$$

Replacing into Eq. (A.24) shows that matrix $\mathbf{A}^{(\ell)}$ is diagonal in this case, with elements given by

$$A_{sn}^{(\ell)}(\omega)=\frac{\beta_n(\omega)}{2\lambda_n^2(\omega)}\{[e^{-\kappa_n(\omega)L_r}-e^{\kappa_n(\omega)L_r}]\kappa_n(\omega)-[e^{-\kappa_n(\omega)L_r}+e^{\kappa_n(\omega)L_r}]\theta_\ell^{(L_r)}(\omega)\}\delta_{sn} \tag{A.28}$$

Replacing Eq. (A.27) into Eq. (A.25), the elements of vector $\mathbf{B}^{(\ell)}$ also simplify to

$$B_s^{(\ell)}(\omega)=\rho_r\eta_\ell H_r\frac{I_{\ell s}(\omega)}{\kappa_s(\omega)}[\kappa_s(\omega)-\theta_\ell^{(L_r)}(\omega)]e^{-\kappa_s(\omega)L_r} \tag{A.29}$$

The solution of the system of equations (A.22) is then obtained as

$$\gamma_{1,n}^{(\ell)}(\omega)=\frac{B_n^{(\ell)}(\omega)}{A_{nn}^{(\ell)}(\omega)}=\frac{2\rho_r\eta_\ell H_r}{\beta_n(\omega)\kappa_n(\omega)}\frac{\lambda_n^2(\omega)I_{\ell n}(\omega)[\kappa_n(\omega)-\theta_\ell^{(L_r)}(\omega)]e^{-\kappa_n(\omega)L_r}}{\{[e^{-\kappa_n(\omega)L_r}-e^{\kappa_n(\omega)L_r}]\kappa_n(\omega)-[e^{-\kappa_n(\omega)L_r}+e^{\kappa_n(\omega)L_r}]\theta_\ell^{(L_r)}(\omega)\}} \tag{A.30}$$

Substituting into Eq. (A.20) and then Eq. (A.15), yields the hydrodynamic pressure

$$\overline{p}_\ell^{(L_r)}(x,y,\omega)=-2\rho_r\eta_\ell H_r\sum_{n=1}^{m_r}\frac{\lambda_n^2(\omega)}{\beta_n(\omega)}\frac{I_{\ell n}(\omega)}{\kappa_n(\omega)}X_{\ell n}^{(L_r)}(x,\omega)Y_n(y,\omega) \tag{A.31}$$

where

$$X_{\ell n}^{(L_r)}(x,\omega)=\frac{e^{\kappa_n(\omega)(x+L_r)}+\zeta_{\ell n}^{(L_r)}(\omega)e^{-\kappa_n(\omega)(x+L_r)}}{e^{\kappa_n(\omega)L_r}-\zeta_{\ell n}^{(L_r)}(\omega)e^{-\kappa_n(\omega)L_r}} \tag{A.32}$$

and

$$\zeta_{\ell n}^{(L_r)}(\omega)=\frac{\kappa_n(\omega)-\theta_\ell^{(L_r)}(\omega)}{\kappa_n(\omega)+\theta_\ell^{(L_r)}(\omega)} \tag{A.33}$$

## References


[1] H.M. Westergaard, Water pressures on dams during earthquakes, *Transactions, ASCE* 98 (1933) 418–472.
[2] A.K. Chopra, Earthquake response of concrete gravity dams, Report No. UCB/EERC-70/01, University of California, Berkeley, CA, 1970.
[3] P. Chakrabarti, A.K. Chopra, Earthquake analysis of gravity dams including hydrodynamic interaction, *Earthquake Engineering and Structural Dynamics* 2 (1973) 143–160.
[4] A.K. Chopra, Earthquake resistant design of concrete gravity dams, *Journal of the Structural Division, ASCE* 104 (1978) 953–971.
[5] J.F. Hall, A.K. Chopra, Two-dimensional dynamic analysis of concrete gravity and embankment dams including hydrodynamic effects, *Earthquake Engineering and Structural Dynamics* 10 (1982) 305–332.
[6] G. Fenves, A.K. Chopra, Earthquake analysis and response of concrete gravity dams, Report No. UCB/EERC-84/10, University of California, Berkeley, CA, 1984.

[7] K.L. Fok, J.F. Hall, A.K. Chopra, EACD-3D, a computer program for three-dimensional earthquake analysis of concrete dams, Report No. UCB/EERC-86/09, University of California, Berkeley, CA, 1986.
[8] S.S. Saini, P. Bettess, O.C. Zienkiewicz, Coupled hydrodynamic response of concrete gravity dams using finite and infinite elements, *Earthquake Engineering and Structural Dynamics* 6 (1978) 363–374.
[9] Ph. Liu, A. Cheng, Boundary solutions for fluid–structure interaction, *Journal of Hydraulic Engineering, ASCE* 110 (1984) 51–64.
[10] C.S. Tsai, G.C. Lee, Arch dam–fluid interactions: by FEM–BEM and substructure concept, *International Journal of Numerical Methods in Engineering* 24 (1987) 2367–2388.
[11] J.L. Humar, A.M. Jablonski, Boundary element reservoir model for seismic analysis of gravity dams, *Earthquake Engineering and Structural Dynamics* 16 (1988) 1129–1156.
[12] J.T. Xing, W.G. Price, M.J. Pomfret, L.H. Yam, Natural vibration of a beam–water interaction system, *Journal of Sound and Vibration* 199 (1997) 491–512.
[13] O. Maeso, J.J. Aznarez, J. Dominguez, Three-dimensional models of reservoir sediment and effects on the seismic response of arch dams, *Earthquake Engineering and Structural Dynamics* 33 (2004) 1103–1123.
[14] Z. Duron, J. Hall, Experimental and finite element studies of the forced vibration response of Morrow Point Dam, *Earthquake Engineering and Structural Dynamics* 16 (1988) 1021–1039.
[15] J. Proulx, P. Paultre, J. Rheault, Y. Robert, An experimental investigation of water level effects on the dynamic behaviour of a large arch dam, *Earthquake Engineering and Structural Dynamics* 30 (2001) 1147–1166.
[16] N. Bouaanani, P. Paultre, J. Proulx, Two-dimensional modelling of ice-cover effects for the dynamic analysis of concrete gravity dams, *Earthquake Engineering and Structural Dynamics* 31 (2002) 2083–2102.
[17] A. Sommerfeld, *Partial Differential Equations in Physics*, Academic Press, New York, 1949.
[18] O.C. Zienkiewicz, R.E. Newton, Coupled vibrations in a structure submerged in a compressible fluid, *International Symposium on Finite Element Techniques*, Stuttgart, 1969.
[19] O.C. Zienkiewicz, D.W. Kelly, P. Bettes, The Sommerfeld (radiation) condition on infinite domains and its modelling in numerical procedures, *Computing Methods in Applied Sciences and Engineering*, Vol. I, 1977, pp. 169–203.
[20] J.T. Xing, Natural vibration of two-dimensional slender structure–water interaction systems subject to Sommerfeld radiation condition, *Journal of Sound and Vibration* 308 (2007) 67–79.
[21] S.S. Saini, Coupled hydrodynamic response of a gravity dam using finite and infinite elements, *Proceeding of the Seventh Symposium on Earthquake Engineering*, Vol. 2, Roorkee, India, 1982, pp. 45–50.
[22] J. Humar, M. Roufaiel, Finite element analysis of reservoir vibration, *Journal of Engineering Mechanics, ASCE* 109 (1983) 215–230.
[23] S.K. Sharan, Finite element analysis of unbounded and incompressible fluid domains, *International Journal of Numerical Methods in Engineering* 21 (1985) 1659–1669.
[24] S.K. Sharan, Finite element modelling of infinite reservoirs, *Journal of Engineering Mechanics, ASCE* 111 (1985) 1457–1469.
[25] S.K. Sharan, A non-reflecting boundary in fluid–structure interaction, *Journal of Computers and Structures* 26 (1987) 841–846.
[26] S.K. Sharan, Efficient finite element analysis of hydrodynamic pressure on dams, *Journal of Computers and Structures* 42 (1992) 713–723.
[27] A.M. Jablonski, Effect of location of transmitting boundary on seismic hydrodynamic pressures on gravity dams, *Proceedings of the Fourth U.S. National Conference on Earthquake Engineering*, Palm Springs, CA, 1990, pp. 95–103.
[28] J. Lysmer, R.L. Kuhlemeyer, Finite dynamic model for infinite media, *Journal of the Engineering Mechanics Division* 95 (1969) 859–877.
[29] Z. Celep, P. Bazant, Spurious reflection of elastic waves due to gradually changing finite element size, *International Journal of Numerical Methods in Engineering* 19 (1983) 631–646.
[30] D. Maity, S.K. Bhattacharyya, Time-domain analysis of infinite reservoir by finite element method using a novel far-boundary condition, *Finite Elements in Analysis and Design* 32 (1999) 85–96.
[31] M. Çetin, Y. Mengi, Transmitting boundary conditions suitable for analysis of dam–reservoir interaction and wave load problems, *Applied Mathematical Modelling* 27 (2003) 451–470.
[32] N. Bouaanani, P. Paultre, A new boundary condition for energy radiation in covered reservoirs using BEM, *Engineering Analysis with Boundary Elements* 29 (2005) 903–911.
[33] D. Maity, A novel far-boundary condition for the finite element analysis of infinite reservoir, *Applied Mathematics and Computation* 170 (2005) 1314–1328.
[34] S. Küçükarslan, An exact truncation boundary condition for incompressible-unbounded infinite fluid domains, *Applied Mathematics and Computation* 163 (2005) 61–69.
[35] I. Gogoi, D. Maity, A non-reflecting boundary condition for the finite element modeling of infinite reservoir with layered sediment, *Advances in Water Resources* 29 (2006) 1515–1527.
[36] N. Bouaanani, P. Paultre, J. Proulx, A closed-form formulation for earthquake-induced hydrodynamic pressure on gravity dams, *Journal of Sound and Vibration* 261 (2003) 573–582.
[37] MATLAB®, The Mathworks, Inc., Natick, MA, USA, 2007.
[38] J.I. Bustamante, E. Rosenblueth, I. Herrera, A. Flores, Presión hydrodinámica en presas y depósitos, *Boletin Sociedad Mexicana de Ingeneria Sismica* 1 (1963) 37–54.
[39] A.K. Chopra, Hydrodynamic pressures on dams during earthquakes, *Journal of the Engineering Mechanics Division, ASCE* 93 (1967) 205–223.
[40] N. Bouaanani, F.Y. Lu, Assessment of potential-based fluid finite elements for seismic analysis of dam–reservoir systems, *Journal of Computers and Structures* 87 (2009) 206–224.
[41] G. Fenves, A.K. Chopra, Simplified earthquake analysis of concrete gravity dams, *Journal of Structural Engineering, ASCE* 113 (1987) 1688–1708.